Target specific routing of visual information by the superior colliculus

Katja Reinhard[1, 2, 3, *], Chen Li[1, 2 *], Quan Do[1, 5], Emily Burke[1, 5], Steven Heynderickx[1, 4] and Karl Farrow[1, 2, 3, 4]

[1] Neuro-Electronics Research Flanders, Leuven, 3001, Belgium.
[2] Department of Biology, KU Leuven, Leuven, 3001, Belgium.
[3] VIB, Leuven, 3001, Belgium.
[4] IMEC, Leuven, 3001 Belgium.
[5] Northeastern University, Boston, MA 02115, USA
* Equal contribution

Summary

The superior colliculus is an important node in the visual system that receives inputs from the retina and distributes these visual features to various downstream brain nuclei. It remains unknown how these circuits are wired to enable specific and reliable information processing. Here the retinal ganglion cells at the beginning of two such circuits, one targeting the pulvinar and the other the parabigeminal nucleus, were labeled using mono-synaptically restricted rabies tracing. Instead of a fuzzy distribution of the retinal outputs, we delineate clear preferences in how information is routed to these two targets. Three retinal ganglion cell types selectively innervated circuits projecting to the pulvinar, six are preferentially routed to the parabigeminal nucleus, and three innervate both circuits. This work argues that neural circuits of the superior colliculus are based on a dedicated set of connections between specific retinal ganglion cell types and different targets of the superior colliculus.

Introduction

The nervous system is built from a large set of diverse neuronal cell types that work together to process information and guide behavior [1]. The neuronal circuits underlying these actions can broadly be divided into two categories. 'Hard-wired' circuits that enable robust and stereotyped behavioral responses [2–4], and flexible networks that modify their computations based on context and experience [5,6]. Many innate behaviors rely on subcortical circuits involving the same well-defined sets of brain structures in different species [7–10]. However, in the visual system it remains unclear to what extent any one brain region has hard-wired rules linking its inputs with its downstream targets [11–16].

The output of the retina encodes over 40 features of the visual scene [17–19]. Each feature is transmitted by a distinct retinal ganglion cell type, which can be distinguished by its dendritic anatomy, response properties, or molecular and genetic markers [17–22]. One of the major retinorecipient areas is the superior colliculus, which receives approximately 90% of the retinal outputs in rodents [16,23–25].

The retinal inputs to the superior colliculus innervate its superficial layers, which consist of several groups of neurons with diverse morphology, visual response properties and mid-brain targets including the lateral pulvinar, lateral geniculate nucleus and parabigeminal nucleus [15,26–30]. Each retino-recipient neuron of the superior colliculus has been estimated to receive input from at least four retinal ganglion cells [31]. Some level of specificity has been demonstrated for direction-selective neurons, which receive input from direction-selective neurons of the retina [32]. However, as projection specific transsynaptic tracing has not been performed it remains unknown what the distribution of ganglion cell types is that synapse onto a group of neurons with a shared projection. This has left unanswered questions about whether each output pathway of the superior colliculus shares a common input logic, and consequently whether the different behaviors initiated by the colliculus are based on different collections of visual features.

To determine the wiring rules by which the retinal output is routed by the superior colliculus to different downstream nuclei, we used a combination of monosynaptic viral tracing and molecular markers to specifically label the retinal ganglion cells at the beginning of two circuits targeting the parabigeminal nucleus (colliculo-parabigmeinal circuit) and the pulvinar (colliculo-pulvinar circuit). Using quantitative analysis of the retinal ganglion cell morphology, we found strong preferences for hard-wired rules governing the routing of visual information through the superior colliculus.

Results

Transsynaptic tracing of retinal ganglion cells from targets of the superior colliculus

To characterize how visual features are routed by the mouse superior colliculus to two distinct brain nuclei, we used viral tools to label the retinal ganglion cells innervating each circuit (Figure 1). This involved injecting either the parabigeminal nucleus (Figure 1A-D) or lateral pulvinar (Figure 1E-H) with a herpes-simplex virus that expressed rabies-G, TVA and mCherry (Figure 1A for parabigeminal nucleus, Figure 1E for pulvinar). In the case of the parabigeminal nucleus, no other target structures of the superficial superior colliculus are in close vicinity [15,26,30]. However, the lateral pulvinar is near the lateral geniculate nucleus, another target of the superior colliculus. To ensure specific infection of neurons

projecting to the lateral pulvinar we used the NSTR1-GN209-Cre mouse line that labels neurons projecting uniquely to the lateral pulvinar [15]. Subsequently, we injected an EnvA-coated rabies virus coding for the fluorescent protein GCaMP6s (EnvA-SADΔG-GCaMP6s) into the superficial layers of the superior colliculus. This transsynaptic viral infection strategy allowed us to specifically express the fluorescent marker GCaMP6s in several dozen retinal ganglion cells per retina that send information to the targeted circuit (Figure 1C and D for parabigeminal nucleus; Figure 1G and H for the pulvinar).

To extract the morphology of single labelled ganglion cells, we stained retinas with antibodies against GFP (binding to the GCaMP6s) and ChAT, which labels starburst amacrine cells (Figure 1I). The dendrites of starburst amacrine cells form two distinct bands in the inner plexiform layer that are commonly used to quantify the dendritic stratification level of retinal ganglion cells [18,33]. We imaged individual ganglion cells with a confocal microscope, creating high-resolution z-stacks of the labelled cell and ChAT-bands. Cells were chosen for analysis if their dendrites showed little overlap with neighbouring cells in the same depth of the inner plexiform layer. Applying a semi-automated routine, we then created a flattened version of the imaged cells [33,34].

The en-face and side-view of the dendrites of 16 example cells are shown in Figure 1J. We extracted the morphology of 146 ganglion cells after injections into the parabigeminal nucleus and 155 cells after lateral pulvinar injections (total: 301 cells from 58 retinas). In this collection, we found a variety of cell morphologies: ~10% of the analyzed cells are bistratified retinal ganglion cells with dendrites at two locations in the inner plexiform layer (n = 31); ~20% are mono-stratified with dendrites below the ChAT-bands (n = 60); ~41% are mono-stratified with dendrites between the ChAT-bands (n = 124); and ~29% were OFF-cells with dendrites stratifying above the ChAT-bands (n = 86). To quantify the morphology of each ganglion cell, we created a density profile of each cell's dendrites relative to the ChAT-bands (Fig S1E) and measured the area covered by the dendrites. Our dataset contains cells with dendritic field diameters of 90 to 420 µm (median: 206 µm, Fig S1F), which is similar to the reported range of 80 to 530 µm [35–38]. The ganglion cells labelled here thus cover the known range of dendritic stratification and size.

Retinal inputs to the parabigeminal and the pulvinar circuit differ in size and stratification

In a first step, we compared the set of retinal ganglion cells that provide input to the parabigeminal and the lateral pulvinar circuits (Figure 2). We found that retinal ganglion cells sending information to the parabigeminal nucleus on average have larger dendritic trees (median: 232 µm) than the cells innervating the colliculo-pulvinar circuit (median: 186 µm; $p < .01$, Kolmogorov-Smirnov test; Figure 2A). Additionally, the lateral pulvinar has a strong bias for retinal ganglion cells stratifying between (50.3%) or above (32.9%) the ChAT-bands and has almost no inputs from bistratified neurons (2.6%; Figure 2B). Approximately 14.2% of neurons are below the ChAT-bands. The parabigeminal nucleus, on the other hand, receives inputs from all four groups of ganglion cells (bistratified 18.5%, below 26.0%, between 31.5%, above 24.0% ChAT-bands; Figure 2B). We show that ganglion cells of the parabigeminal circuit are generally larger at all dendritic stratification depths (below ChAT-bands: 280 µm (parabigeminal) vs 183 µm (pulvinar); between ChAT-bands: 185 µm vs 130 µm; above ChAT-bands: 234 µm vs 170 µm; Figure 2C). In each of these anatomical divisions the size distributions and medians are statistically different ($p < .01$; Kolmogorov-Smirnov test and Wilcoxon rank sum test).

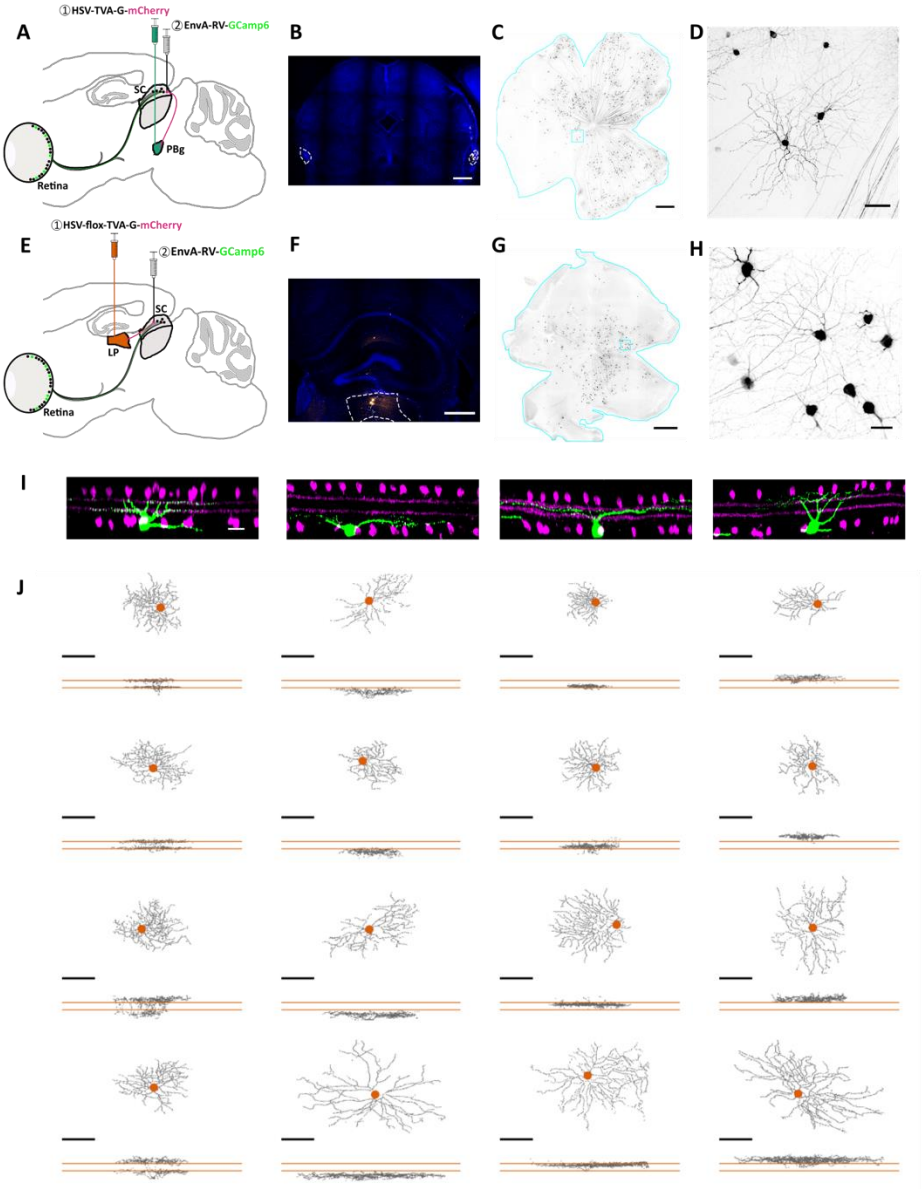

Figure 1: Transsynaptic tracing of retinal ganglion cells from the parabigeminal nucleus and the lateral pulvinar. A-D) Labelling of the inputs to the parabigeminal nucleus circuit. **A)** Injection strategy for viral labelling of the circuit that connects the retina via the superior colliculus to the parabigeminal nucleus. **B)** Histological section after parabigeminal nucleus injection. The pipette was coated with a fluorescent dye (DiD), and the fluorescent signal coincides with the location of the parabigeminal nucleus indicated with a dashed box. **C)** Example retina with labelled ganglion cells innervating the colliculo-parabigeminal circuit. **D)** Zoomed-in version of C showing the morphology of a few labelled ganglion cells. **E-H)** Labelling of the inputs to the pulvinar circuit. Analogous to A-D. Scale bar = 500 µm (B, C, F, G), Scale bar = 50 µm (D, H) **I-J)** Overview of retinal ganglion cells in the two circuits. **I)** Side-view of z-stack scans of four example retinal ganglion cells (green) and the ChAT-bands (magenta). Scale bar = 20 µm. **J)** 16 retinal ganglion cells from either injection approach (parabigeminal nucleus or pulvinar). Top: en-face view of the dendritic tree. Bottom: side-view of the dendritic tree. Location of ChAT-bands is indicated with two orange lines. The cells have been broadly separated into four stratification groups: bistratified (first column), below ChAT-bands (second column), between ChAT-bands (third column), and above ChAT-bands (last column).

98

To determine if these differences are due to a bias in the retinotopic location of the sampled ganglion cells, we checked the spatial distribution across the retina of the labeled neurons. For each circuit we sampled from all retinal quadrants at various eccentricities (Figure 2D-F). 33% of labelled ganglion cells were sampled from the central third of the retina (between 0 µm and 833 µm from the optic nerve; 1.5 cells per 10^5 µm^2), 53% from the middle third (between 833 µm and 1667 µm from the optic nerve; 0.8 cells per 10^5 µm^2) and 14% from the peripheral third (between 1667 µm and 2500 µm from the optic nerve; 0.1 cells per 10^5 µm^2). Further, we sampled 25% of all cells from the upper left quadrant (naso-dorsal), 27% from the upper right (dorso-temporal), 21% from the lower right (temporo-ventral) and 27% from the lower left quadrant (ventro-nasal). This indicates that the observed difference in size between the two circuits is not due to a sampling bias in retinotopic location.

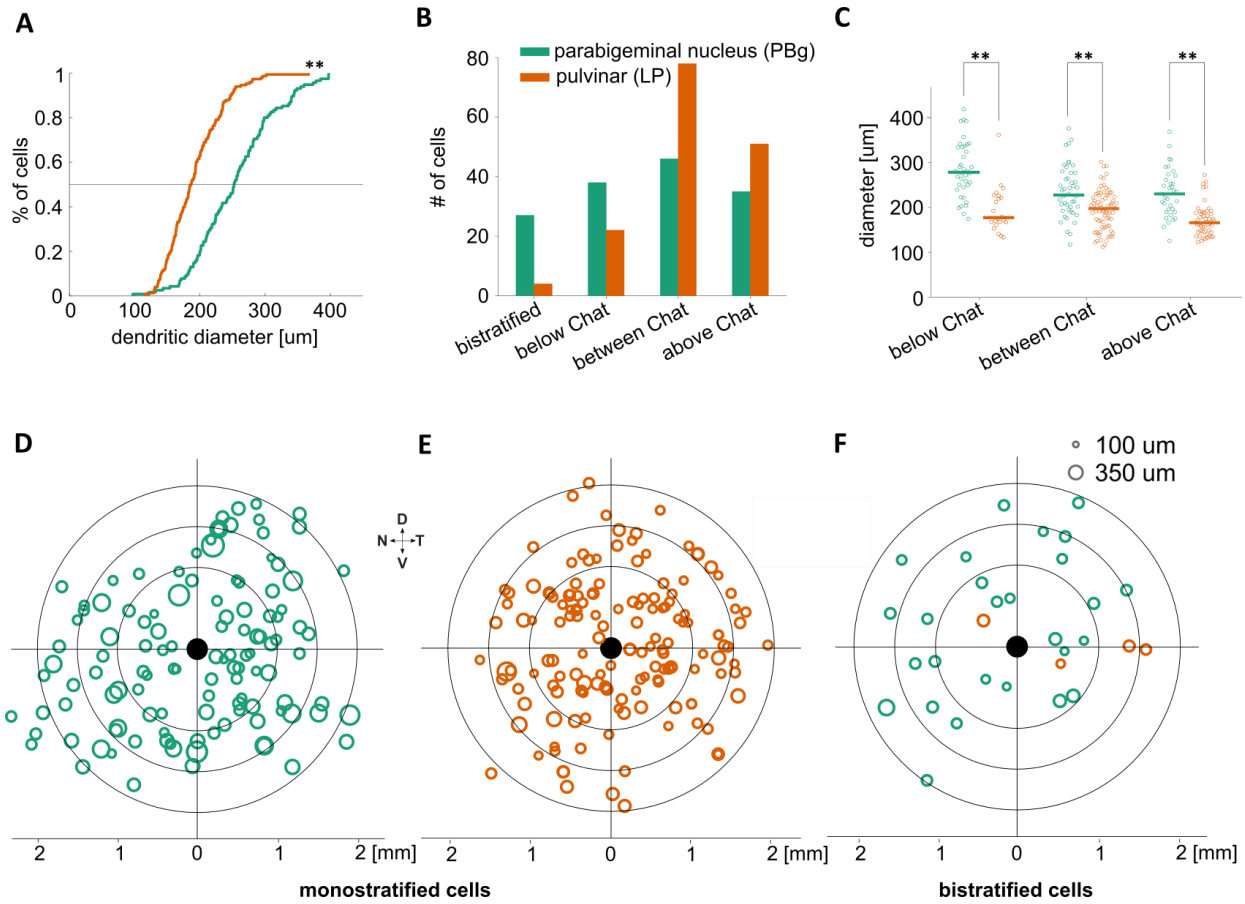

Figure 2: Size and stratification differences of retinal ganglion cells. A) Distribution of dendritic tree diameter of retinal ganglion cells that are part of the pulvinar (orange) and the parabigeminal nucleus (green) circuit. ** = p < .01 Kolmogorov-Smirnov test. **B)** Retinal ganglion cells of each circuit were grouped into four stratification groups based on the peak of their dendritic profile. **C)** Retinal ganglion cell diameters for cells stratifying below, between, and above ChAT-bands. ** = p < .01 Kolmogorov-Smirnov test and Wilcoxon rank sum test. **D-F)** Retinal position and dendritic tree diameter of retinal ganglion cells that are part of the parabigeminal nucleus circuit (D), cells innervating the colliculo-pulvinar circuit (E), and bistratified ganglion cells of both circuits (F). N = nasal, D = dorsal, T = temporal, V = ventral. The optic nerve is indicated with a black disc.

Retinal inputs to the parabigeminal and the pulvinar circuit differ in molecular signature

To identify the types of retinal ganglion cells in our dataset, we performed histological staining against known molecular markers of ganglion cell types. One set of retinal ganglion cells that can be labelled using antibodies are the alpha cells, which in mice form a group of four ganglion cell types that can be distinguished based on their dendritic stratification and labeling using SMI32-antibodies against neurofilament [35,39–42] . This group of neurons contains two ON and two OFF cells that include: a sustained ON-type lying just below the ChAT-bands; a transient ON- and transient OFF-type stratifying between the ChAT-bands and a sustained OFF-type with dendrites above the ChAT-bands [40]. We found that around half of all rabies-labelled cells innervating the parabigeminal (median: 42%, range: 41 to 53%, n = 3 retinas; Figure 3A-C), and the pulvinar circuits (median: 53%, range: 45 to 56%, n = 4 retinas; Figure 3E-G) are alpha-cells (SMI32$^+$). To identify which of the four alpha cell types are part of each circuit, we acquired local z-stacks of 91 SMI32$^+$/GCaMP6s$^+$ double labeled neurons from 3 parabigeminal experiments, and 90 SMI32$^+$/GCaMP6s$^+$ cells from 3 pulvinar experiments. Each neuron was manually grouped into one of the four types based on its dendritic stratification depth (Figure 3D and 3H). We found that each circuit samples from sustained OFF-alpha cells: in parabigeminal experiments, 13% of all SMI32$^+$ cells are sustained OFF-cells (range: 12 to 43%); in the pulvinar experiments, 29% weraree sustained OFF-cells (range: 14 to 54%). Similarly, both circuits receive inputs from transient OFF-cells (parabigeminal nucleus median: 32% range: 10 to 53%; pulvinar median: 29%, range: 27 to 41%). In contrast, transient ON-cells show a very strong preference for innervating neurons projecting to the pulvinar (parabigeminal nucleus median: 4% range: 0 to 10%; pulvinar median: 17%, range: 0 to 31%), while sustained ON-cells are almost exclusively labelled after parabigeminal injections (parabigeminal nucleus median: 10%, range: 0 to 33%; pulvinar median 0%, range: 0 to 4%).

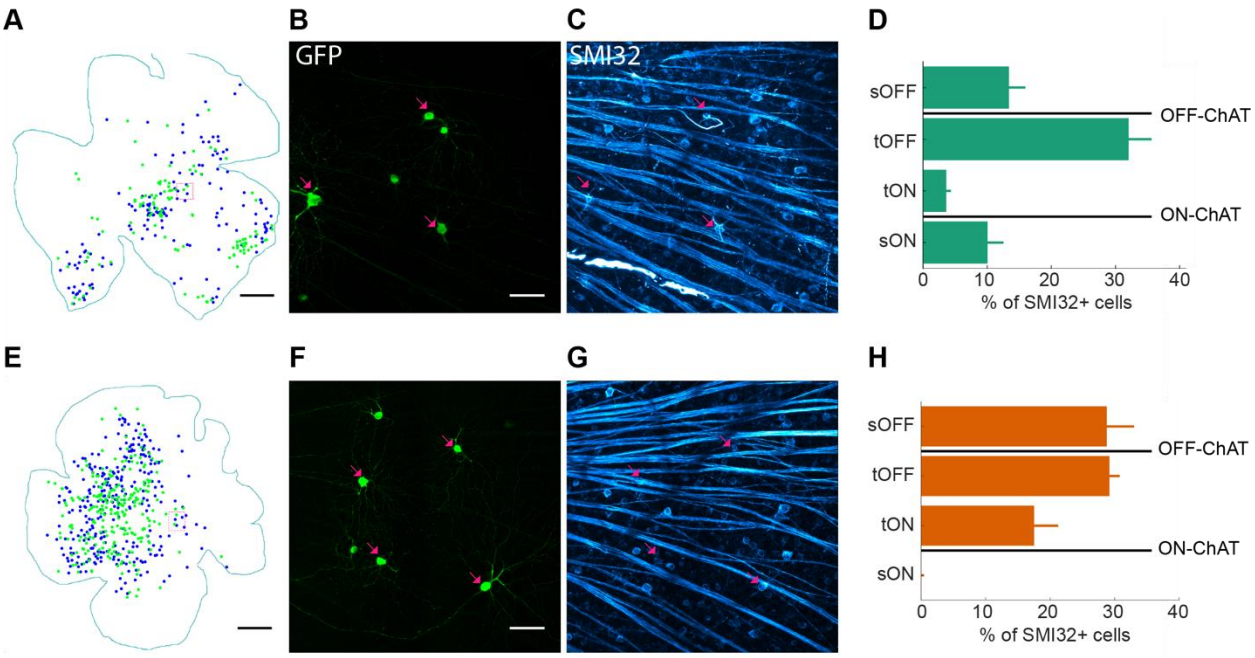

Figure 3: Distinct projection patterns of alpha retinal ganglion cells. A-D) Alpha retinal ganglion cells sending information to the colliculo-parabigeminal circuit. **A)** Schematic of example retina with SMI32-negative labelled retinal ganglion cells (non-alpha cells labelled after parabigeminal injections; green) and SMI32-positive labelled retinal ganglion cells (alpha cells providing input to the parabigeminal circuit; blue) from n = 3 retinas. **B)** Zoomed-in version of A showing histological staining of all labelled retinal ganglion cells in this region (anti-GFP). **C)** SMI32-staining in the same region. Arrows indicate double-labelled ganglion cells. **D)** Median percentage of the four different alpha ganglion cell types (100% corresponds to all GCaMP6s-expressing cells). n = 91 cells from 3 retinas. Bars indicate standard errors. **E-H)** Alpha retinal ganglion cells sending information to the colliculo-pulvinar circuit. Analogous to A-D. n = 4 retinas for E and n = 90 cells from 3 retinas for H. Scale bar = 500 µm (A,E), scale bar = 50 µm (B,C,F,G).

In our dataset, the bistratified cells with density peaks on the two ChAT-bands strongly resemble the morphology of ON-OFF direction-selective cells [18]. In the mouse retina, there are four types of ON-OFF direction-selective ganglion cells, each responding specifically to one of the four cardinal directions. Three out of the four types can be labelled with anti-CART antibodies [43]. We performed anti-CART histological staining in a subset of the retinas from both experimental assays (Figure 4). Double labeled neurons (GCaMP6s and CART) are found almost exclusively only after retrograde tracing from the parabigeminal nucleus (median: 6.9% of all GCaMP6s-postive cells, range: 4.3 to 9.1%, n = 3 retinas). In the pulvinar experiments, a negligible percentage of the labelled ganglion cells are $CART^{+}$ (median: 1.3%, range: 0 to 2.1%, n = 6 retinas). In two of the retinas we saw no double labeled neurons (0/34 and 0/536).

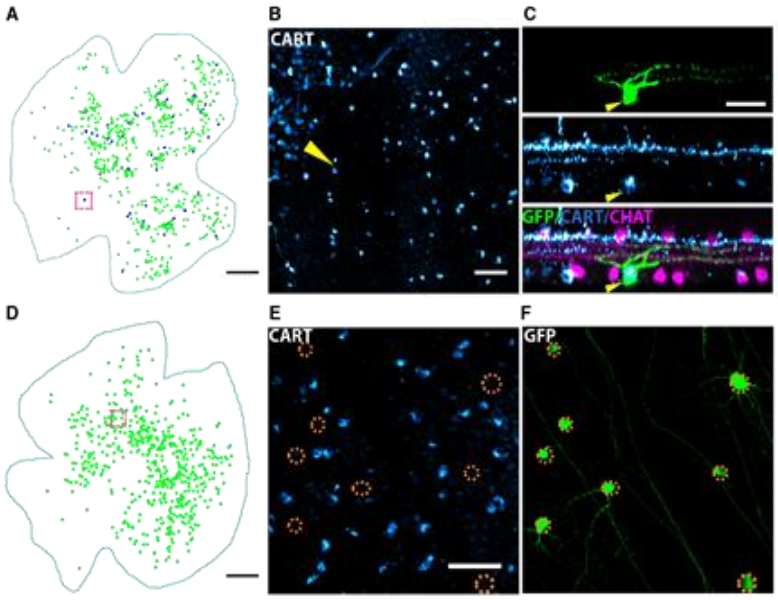

Figure 4: ON-OFF direction-selective cells provide input to the parabigeminal nucleus. A-C) ON-OFF direction-selective cells innervating the colliculo-parabigeminal circuit. **A)** Schematic of example retina with CART–positive labelled retinal ganglion cell (ON-OFF direction-selective cells providing input to the parabigeminal circuit; blue) and CART-negative labelled retinal ganglion cells (other retinal ganglion cells labelled after parabigeminal injections; green). **B)** Histological staining against-CART of region marked in A. The arrow indicates a double-labelled cell (GFP signal not shown) **C)** Side-view of the cell labelled in B. The cell has been labelled by the rabies virus (GFP-positive; top) and is CART-positive (middle). Bottom: overlay of GFP, CART, and ChAT-staining. **D-F)** Numbers of ON-OFF direction-selective cells are negligible in the pulvinar circuit. **D)** Schematic of example retina stained with anti-GFP to label the retinal ganglion cells (green). None of the GFP-positive cells is CART–positive. **E)** Histological staining against CART of the area marked in D. **F)** Histological staining against GFP of the same region as in E. The region contains 8 rabies-infected cells. Scale bar = 500 µm (A,D), Scale bar = 50 µm (B,E,F), Scale bar = 20 µm (C).

Distinct routing of a small set of retinal features to the parabigeminal and the pulvinar circuit

To characterize the rules by which circuits of the superior colliculus projecting to the parabigeminal nucleus and the pulvinar sample retinal inputs, we clustered our morphological data taking into consideration information about molecular identity. This allowed us to know the molecular identity of 54 out of the 301 ganglion cells in our data set (n = 51 for SMI32; n = 3 for CART). We first set the average dendritic stratification profile for each genetically identified cell type as a cluster centroid (4 SMI32^{+} types and 1 CART^{+} group). Then, all cells were clustered using an affinity-propagation based algorithm [44]. This resulted in 12 clusters based on three validation indices (Figure 5A). Figure 5B shows a low-dimension visualization of the separation of cells within the different clusters computed using tSNE [45]. This visualization shows that each cluster forms a separate group. The second tSNE dimension separates the cells based on their dendritic stratification peak so that OFF-cells (light green, dark green, black) are clearly separated from ON-cells (rose, violet, purple) and cells stratifying between the ChAT-bands (yellow, light orange, dark orange, red). tSNE dimension 1 separates the bistratified cells (light and dark blue) from ON-cells, while dimension 3 highlights the separation of clusters within the big groups (ON, OFF, bistratified, between ChAT-bands).

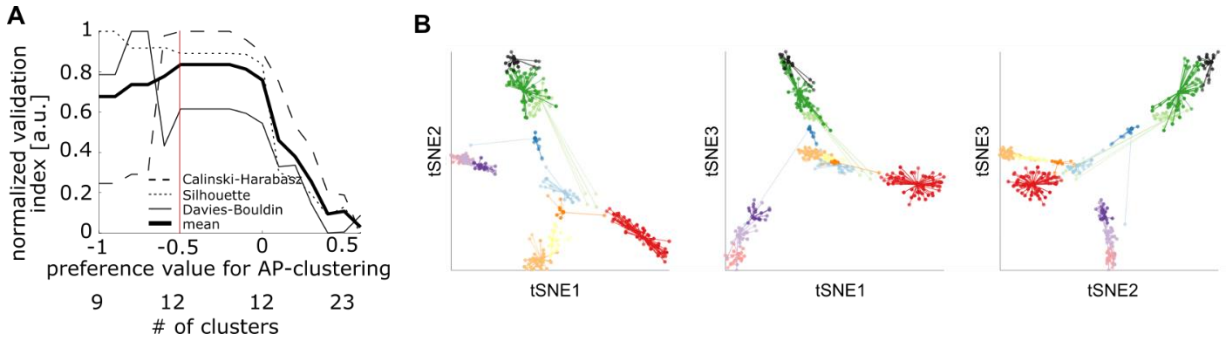

Figure 5: Validation and visualization of dendritic stratification clustering. A) Validation of clustering result. Three normalized validation indices (Calbinski-Harabasz, Silhouette, Davies-Bouldin) and their mean is shown. The clustering result taken for further analysis is marked with a red line. **B)** Visualization of the cells in the 12 clusters using t-distributed stochastic neighbor embedding (tSNE). Each plot shows the distances between individual data points. Transparency of the lines shows the similarity between two data points based on the affinity-propagation clustering. Colors indicate different clusters.

Figure 6 shows the dendritic density distribution and example cells for the resulting 12 putative retinal ganglion cell types, together with 3 example cells from each cluster. Numbers indicate the percentage of retinal ganglion cells for each circuit that were grouped into each cluster as well as absolute numbers of cells in the cluster. We found three distinct groups of cell types: 6 types that send information mostly to the parabigeminal circuit, 3 clusters that are almost exclusively part of the pulvinar circuits, and 3 types that are shared by the two circuits. Taken together, the colliculo-pulvinar and the colliculo-parabigeminal circuits sample from a small and only partially overlapping set of retinal ganglion cell types.

The cells that are innervating predominantly the colliculo-parabigeminal circuit include six putative types: cluster 1, 2, 3, 4, 7, and 12. These clusters included both bistratified types: Cluster 1 contains the CART$^+$ cells and consists of rather small ganglion cells with two stratification layers that overlap with the ChAT-bands (n = 21; median diameter: 198 µm). These ganglion cells resemble the ON-OFF direction selective cells that are CART$^+$, co-stratify with the ChAT-bands and have relatively small dendritic fields [18]. In cluster 2 we find another type of bistratified cell with a larger dendritic tree that stratifies below the ON-ChAT-band and above the OFF-ChAT-band (n = 10; median diameter: 214 µm). Two clusters contain ON-neurons stratifying below the ON-ChAT-band. One of the ON-types (cluster 4) contains SMI32$^+$ cells (n = 22; median diameter: 276 µm), and has a morphology similar to sustained ON-alpha cells [39,40]. The very strong bias of this cluster for the parabigeminal circuits mimics our antibody-labeling results of SMI32$^+$ cells (Figure 3D and H). The second ON-type (cluster 3) does not contain SMI32$^+$ cells, stratifies further away from the ON-ChAT-band and has a smaller dendritic tree (n = 18; median diameter: 232 µm). A single cluster (cluster 7) has neurons stratifying between the ChAT-bands. These cells have relatively small dendritic trees that are located closer to the ON than the OFF-ChAT band (n = 16; median diameter: 185 µm). The last cell type that specifically targets the parabigeminal circuits consists of

relatively large OFF-cells stratifying far above the OFF-ChAT-band (cluster 12, n = 19; median diameter: 243 µm).

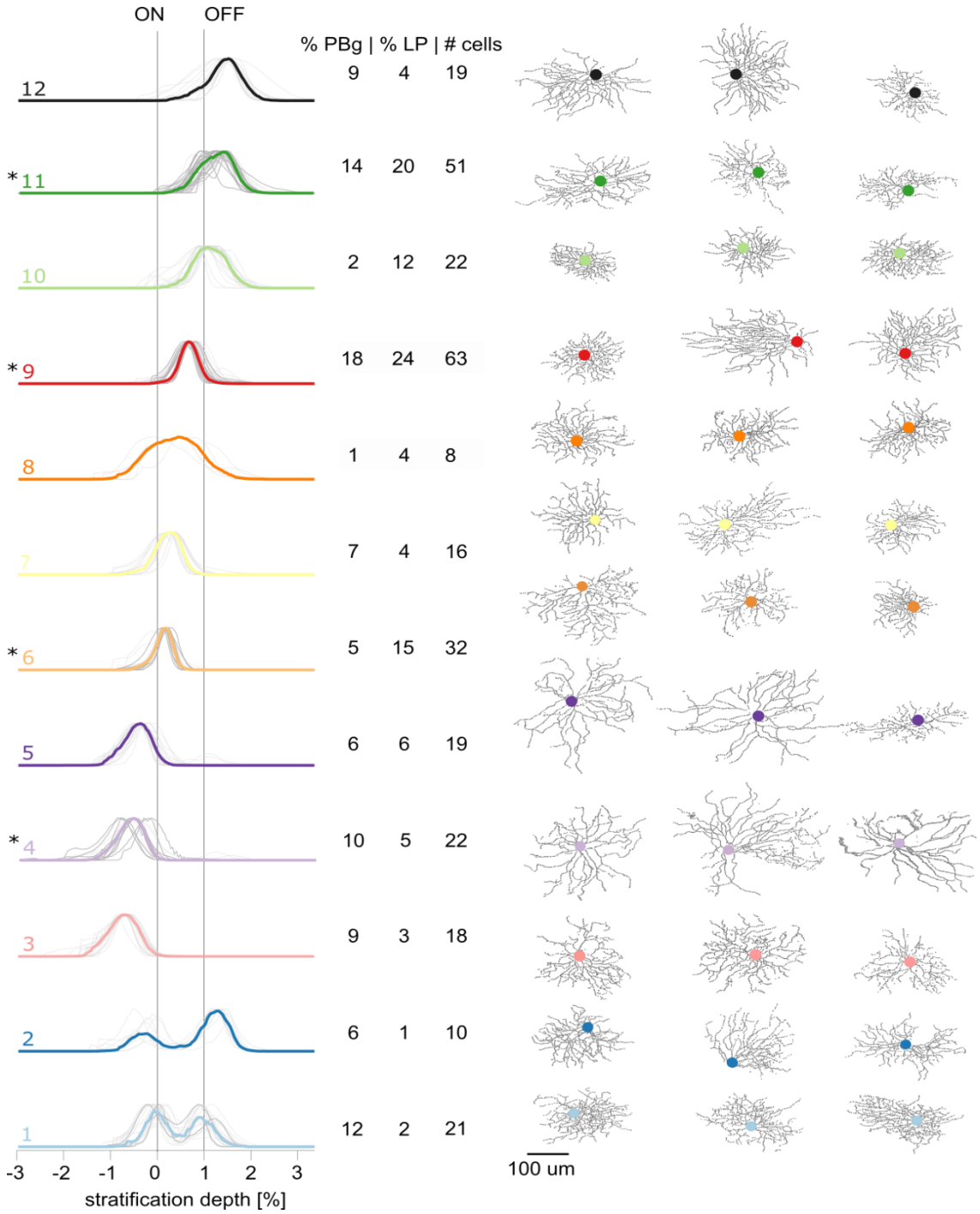

Figure 6: Retinal ganglion cell types targeting parabigeminal- and pulvinar-projecting collicular neurons. A) 12 clusters resulting from affinity propagation clustering based on the morphology and molecular markers of 301 retinal ganglion cells. Left: dendritic stratification profiles (median in color). Profiles for individual cells are plotted in light gray if the molecular identity is unknown and in darker gray if it is either CART- or SMI32-positive. Numbers indicate percentages of ganglion cells in a given cluster that were labelled after parabigeminal nucleus or pulvinar injections and the total number of cells in each cluster. * Indicates clusters with SMI32-positive cells. Right: en-face view of 3 example cells for each cluster that are the most similar to the cluster median.

The three ganglion cell types sending information preferentially to the pulvinar via the superior colliculus are in cluster 6, 8, and 10 and do not include any bistratified cells. Cluster 6 consists of ganglion cells stratifying just above the ON-ChAT-band and contains SMI32$^+$ neurons (n = 32; median diameter: 176 µm), which resemble the transient ON-alpha cell [40]. The selective routing of this type to the pulvinar is consistent with the molecular labeling experiments where transient ON-alpha cells are mostly labelled after pulvinar injections (Figure 3D and H). The cells in cluster 8 have an exceptionally broad dendritic tree and small dendritic fields (n = 8; median diameter: 199 µm). The third type of ganglion cells that targets uniquely the colliculo-pulvinar circuit is a rather small OFF-type stratifying just above the OFF-ChAT-band (cluster 10, n = 22; median diameter: 166 µm).

Finally, three clusters send information to both collicular targets (cluster 5, 9 and 11). An ON-type (cluster 5) stratifies just below the ON-ChAT-band and has a sparse dendritic tree (n = 19; median diameter: 249 µm). Cluster 9 contains SMI32$^+$ cells (n = 63; median diameter: 230 µm) with relatively large dendritic trees just below the OFF-ChAT-band that resemble the morphology of transient OFF-alpha cells [40,42,46]. SMI32$^+$ cells can also be found in cluster 11 (n = 51; median diameter: 187 µm). These OFF-cells stratify above the OFF-ChAT-band and are smaller in size, comparable to the published morphology of sustained OFF-cells [39,40,47]. These results are consisted with our analysis of SMI32$^+$ neurons (Figure 3D and H) where we found that both transient and sustained OFF-cells are labelled after parabigeminal and pulvinar injections.

Dendritic field size variability within clusters is consistent with known retinotopic differences

To determine if any individual cluster likely contains more than one cell type we looked at the stratification and size variances within each group. This might be the case as to cluster the retinal ganglion cells we only considered differences in the depth profile of their dendritic trees, but not details of the xy-morphology such as dendritic field size. The dendritic field size can vary substantially between cells of a given cluster (Figure 7B), where generally smaller cells have a narrower range of dendritic diameters (e.g. cluster 6 and cluster 10), while larger cells span a broader range of sizes (e.g. cluster 5 and cluster 12). To determine if this variability is comparable to that of other cell types we compared it to data from 8 parvalbumin-positive ganglion cells [47]. We found that both the median size and variability corresponds to the observed range of dendritic tree sizes (Figure 7C). Both the range of sizes of stratification- and size-matched pairs is comparable between our dataset and the parvalbumin-cells as well as the trend of increasing variability for cells with bigger dendritic trees.

To further investigate that the differences in size within a cluster are within the expected range, we compared the size distribution of alpha-cell clusters with those previously reported [39,40]. When considering all 301 labelled cells, we find that cells in the central retina tend to be smaller than in the periphery (Figure 7D). This is consistent with the observation that cells in the central mouse retina are more densely packed than in the periphery [39,48,49]. Additionally, sustained alpha-cells have been show to have a distinctive retinotopic size distribution [39]. We found in our data set that putative sustained alpha-cells (ON and OFF, cluster 4 and 11) are smaller in the temporal part of the retina as compared to the dorsal part (Figure 7E; Spearman-correlation: $r = -0.43$, $p \sim 0.001$; Pearson-correlation: $r = -0.33$, $p \sim 0.004$), but do not change significantly in size with eccentricity (Spearman-correlation: $r = 0.07$, $p \sim 0.58$; Pearson-correlation: $r = 0.13$, $p \sim 0.27$). This is the same trend as reported previously for dendritic

diameters of sustained ON- and OFF-alpha cells [39]. In contrast, the size distribution of transient OFF-alpha cells is much more homogeneous and centered (Figure 7F; Spearman-correlation nasal-temporal: r = -0.16, p ~0.21; Pearson-correlation nasal temporal: r = -0.12, p ~ 0.33; Spearman-correlation eccentricity: r = 0.21, p ~0.102; Pearson-correlation eccentricity: r = 0.22, p ~ 0.086), which is consistent with published observations [39].

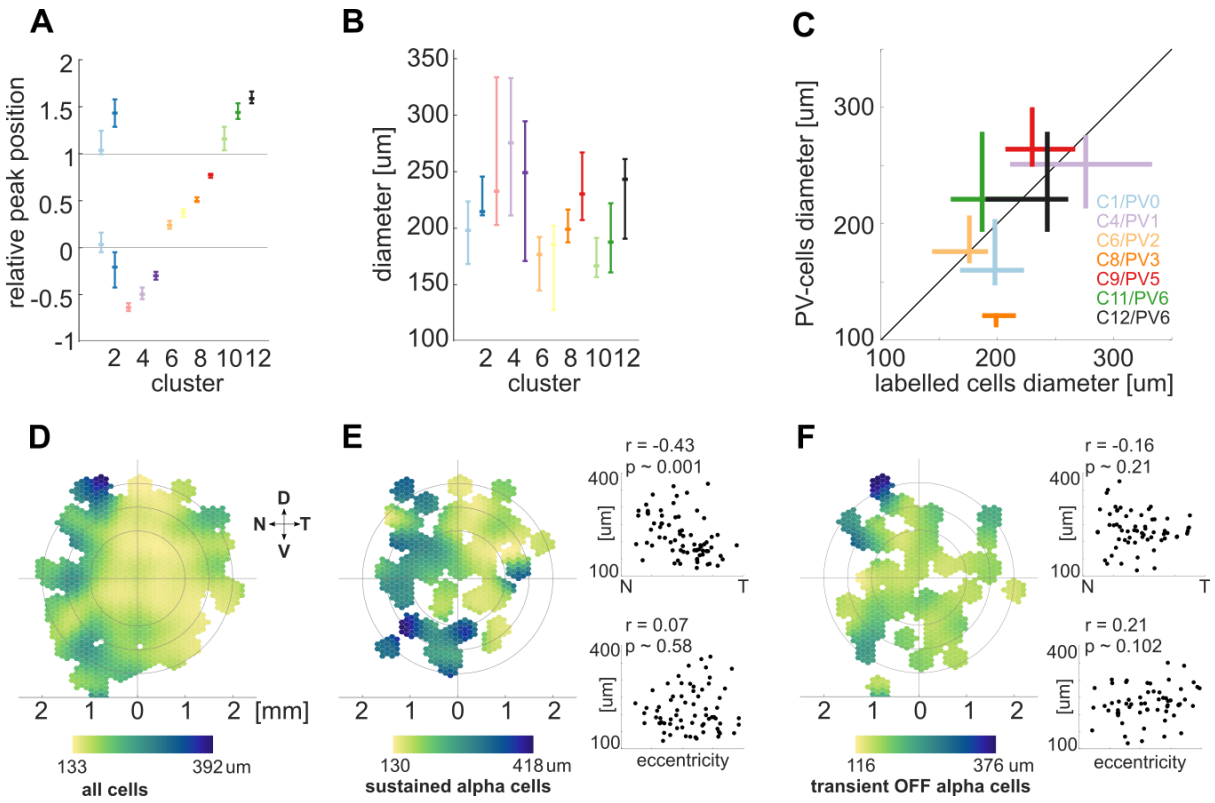

Figure 7: Dendritic tree size variability. **A)** Peak of stratification profile for each cluster (median and quartiles). **B)** Dendritic tree diameter for cells in each cluster (median and quartiles). **C)** Cell diameter median and quartiles of 7 clusters and the corresponding parvalbumin-positive (PV) cells [47] that have a similar stratification depth and similar average size. **D)** Smoothed distribution of dendritic field diameter of all labelled cells (n = 301) at their retinotopic location**. E)** Smoothed distribution of dendritic field diameter of all cells in the sustained alpha clusters (n = 22 sustained ON-cells in cluster 4 and n = 51 OFF-cells in cluster 11)**.** Top right: dendritic field size along the naso-temporal axis. Spearman-correlation: r = -0.43, p ~0.001; Pearson-correlation: r = -0.33, p ~ 0.004. Bottom right: dendritic field size relative to eccentricity (from optic nerve to periphery). Spearman-correlation: r = 0.07, p ~0.58; Pearson-correlation: r = 0.13, p ~ 0.27. **F)** Smoothed distribution of dendritic field diameter of the cells in the transient OFF-alpha cluster (n = 63 in cluster 9). Top right (naso-temporal axis): Spearman-correlation: r = -0.16, p ~0.21; Pearson-correlation: r = -0.12, p ~ 0.33. Bottom right (eccentricity): Spearman-correlation: r = 0.21, p ~0.102; Pearson-correlation: r = 0.22, p ~ 0.086.

Discussion

We used transsynaptic viral tracing to investigate the rules by which visual features extracted by the retina are routed in two neuronal circuits passing through the superior colliculus. We found that the two circuits sample from a limited and only partially overlapping set of retinal output neurons (Figure 6). These results support the notion that, in the superior colliculus, neural circuits are based on a dedicated set of connections between specific retinal output neurons and different collicular output pathways.

Clustering of morphological and molecular marker parameters of retinal ganglion cells lead us to three main conclusions. First, our data suggests that the colliculo-parabigeminal and colliculo-pulvinar circuits together receive inputs from 12 different ganglion cell types (Figure 6). Second, we observed a clear segregation in the retinal ganglion cell types providing input to the two circuits. Six of the twelve putative ganglion cell types showed a strong preference for the parabigeminal circuit, and three clusters a strong bias for the pulvinar circuits (Figure 6 and Table 1). This finding indicates that the two circuits sample, at least partially, from different aspects of the visual scene. Finally, there is a set of 3 visual features that provide input to both circuits.

We used a combination of morphological and molecular cues to link the 12 clusters to known retinal ganglion cell types (Table 1). For instance, the cells in cluster 1 are ON-OFF direction-selective cells [18,43]

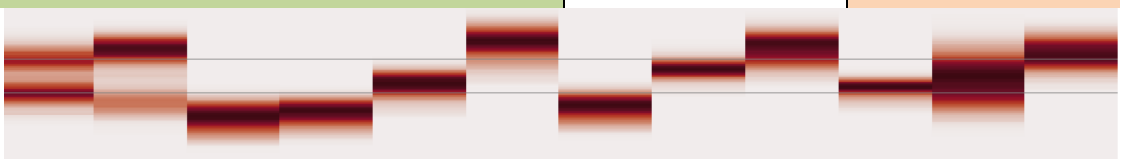

	Parabigeminal nucleus						Shared			Pulvinar		
Cluster #	1	2	3	4	7	12	5	9	11	6	8	10
Molecular Marker	CART			SMI32				SMI32	SMI32	SMI32		
Putative Type	ONOFF-DS[1-4]	ON-vOS[5]	C[3]	sONa[1,2,4]	G5[6]	Z[3]	U[3] G10[6]	tOFFa[1-4]	sOFFa[1,2] W7B[4]	tONa[1,2,7] X[3]	ONOFF-local-OS[1] W3[2,4] E[3] G8[6]	OFF-hOS[8]
Putative Function	Movement direction	Vertically oriented objects	?	Large moving objects	?	?	?	Expansion detector	Large moving objects	Small objects	Local motion	Horizontally oriented objects

[1] Baden et al. 2016, [2] Farrow et al. 2013, [3] Sümbül et al. 2014, [4] Dhande et al. 2015, [5] Nath & Schwartz 2016, [6] Völgyi et al. 2009, [7] Krieger et al. 2017, [8] Nath & Schwartz 2017

Table 1: Putative retinal ganglion cell types and function. Main target, median dendritic stratification pattern, molecular markers, putative type and function of the 12 retinal ganglion cells. Names refer to cluster names in the corresponding references. DS = direction-selective; vOS = vertical orientation-selective; sONa = sustained ON-alpha; tOFFa = transient OFF-alpha; sOFFa = sustained OFF-alpha; tONa = transient ON-alpha; hOS = horizontal orientation-selective.

and the four alpha ganglion cell types are represented by cluster 4 (ON sustained), 6 (ON transient), 9 (OFF transient), and 11 (OFF sustained) [39,40]. To match the other clusters to known ganglion cell types we compared the morphology – stratification and size – with known genetically, morphologically and functionally defined cell-types. Based on these criteria, the second bistratified cluster 2 is most similar to recently identified ON vertical orientation-selective neurons [50]. A second cluster with striking anatomical characteristics is cluster 8, containing cells that resemble the “W3” cell, otherwise known as the “local-edge detector” or “object motion selective” cell [29,33,47,51]. The small, dense OFF-cells in cluster 10 have a passing resemblance to horizontal OFF orientation-selective neurons [52]. There are three additional clusters that resemble cell types described by Sümbül and colleagues in terms of stratification pattern, size and dendritic density [33]. First, the relatively dense ON-cells in cluster 3 have a similar morphology as the Kb-cells. Second, the larger OFF-cells in cluster 12 are similar to Z-cells. These two cells have not yet been associated with visual response properties. Cluster 5 cells are large ON-cells with a sparse dendritic tree. They resemble the cells provisionally labelled as "U" by Sümbül and colleagues and the G10-cell by Völgyi and colleagues [33,53]. Finally, the cells in cluster 7 stratifying just above the ON-ChAT-band show a similar profile as G5-cells [53].

The two neural circuits investigated here are each known to mediate visually guided aversive behaviors [26,27]. In this context, the details of the encoded visual features by the ganglion cells innervating those circuits are of interest. We have identified 5 putative functional ganglion cell types and have good indications for the identity of another 3 (Table 1). The $CART^+$ ON-OFF direction-selective cells in cluster 1 inform the brain about objects moving in specific directions. Further, the two sustained alpha ganglion cell types (cluster 4 and 11) respond preferentially to large, fast moving objects of positive or negative contrast, respectively [40,47,54]. The transient ON-alpha cells (cluster 6), in contrast, prefer small stimuli [40]. The fourth alpha-type, the transient OFF-alpha cells (cluster 9), have been shown to selectively respond to approaching stimuli [46]. Due to their resemblance to the local-edge / object-motiont detector [17,51], cells in cluster 8 most probably send information about local motion to the superior colliculus. Finally, two cell types in our dataset are potential orientation-selective cells, with a preference for vertical objects for cells in cluster 2 [50] and for horizontal objects in cluster 10 [52].

If we consider the putative ganglion cell types of each circuit separately, we find that the pulvinar circuit receives input from neurons with smaller dendritic fields that tend to stratify closer to the OFF-ChAT-band (Figure 2). Dendritic size is closely related to receptive field size and we see a similar preference for small, local stimuli in the putative functional ganglion cell types that were selectively labelled in pulvinar experiments (cluster 6 and 8). This finding is also in accordance with the stimulus preferences of pulvinar-projecting neurons in the superior colliculus [15,55]. The parabigeminal circuit, on the other hand, samples more evenly from ON, OFF and ON-OFF neurons with a larger average dendritic field (Figure 2). In agreement with the morphological data, the putative functional ganglion cell types that were specifically labelled in parabigeminal experiments inform this circuit about larger moving objects and their movement direction (cluster 1 and 4). It is noteworthy that both circuits receive input from transient OFF-alpha cells which are known to preferentially respond to expanding stimuli. Such a stimulus would be created, for instance, by an approaching predator. This is in accordance with robust responses to such

expanding stimuli in both pulvinar-projecting [55] and parabigeminal nucleus-projecting neurons [26] of the superior colliculus.

There are some limitations to our study. First, the rabies virus might have a bias in its infection of different cell types. To mitigate this, we expressed the TVA-receptor in collicular neurons and coated the rabies virus with its ligand EnvA. This approach should decrease biological variability in infection rates [56]. The fact that we sample from different ganglion cell types and with very different distributions in both experimental paradigms speaks against a strong infection bias of the herpes-simplex or rabies virus. Another bias may arise from the injection locations and the choice of ganglion cells that we imaged. We do not know the retinotopic location of the first injection into the pulvinar or the parabigeminal nucleus. However, in most retinas, a large proportion of the retina contained labelled cells and our dataset contains cells from all retinal quadrants and eccentricities (Figure 2D-F). Furthermore, we did not select cells for imaging based on morphological features but looked for cells that were isolated enough to allow for extraction of their dendritic tree.

Studies investigating the organization of retinal inputs to single cells in the lateral geniculate nucleus have suggested that there is a large degree of fuzziness/variability in the information each neuron receives from the retina [11,13,57]. Here we demonstrate that in the superior colliculus a high degree of regularity exists if one considers the projection targets. These differences could exist either because this study was performed in the superior colliculus, which might have a more hard-wired architecture; or because we focused on projection specific disynaptic circuits instead of comparing input to single neurons. When considering the layer specific targets of the lateral geniculate nucleus in the visual cortex Cruz-Martin et al. suggest that direction-selective neurons are selectively sampled [12]. In order to understanding the rules by which neurons sample information it is clearly necessary to consider the projection profile of individual neurons and cell types [15,58].

Acknowledgements

We thank Keisuke Yonehara for supplying the NSTR-GN209-Cre mice, as well as Norma Kühn and João Couto for reading the manuscript. Grants are as follows: Marie-Curie CIG (631909) and FWO Research Project (G094616N) to K.F. This project has received funding from the European Union's Horizon 2020 research and innovation programme under the Marie Skłodowska-Curie grant agreement No 665501 to K.R. (12S7917N). C.L. is funded by the Chinese Scholarship Council.

Contributions

K.R. and C.L. performed experiments, analysed the data and wrote the manuscript. Q.D. implemented automated method for ChAT band detection. E.B. performed experiments. S.H. established viral production facility. K.F. analysed the data and wrote the manuscript.

METHODS

EXPERIMENTAL MODEL AND SUBJECT DETAILS

40 mice (3-5 weeks old) of either sex were used in our experiments including PvalbCre, PvalbCre x Ai9, Ntsr1-GN209Cre and Ntsr1-GN209Cre x Ai9. PvalbCre mice (JAX: 008069) [59] express Cre recombinase in parvalbumin-expressing neurons. Ntsr1-GN209Cre mice (Genset: 030780-UCD) express Cre recombinase in Ntsr1-GN209-expressing neurons. Ai9 (JAX: 007909) is a tdTomato reporter mouse line [60]. Animals were maintained on a 12-hour light/dark cycle, and fed with sterilized food, water, bedding and nesting material. All animal procedures were performed in accordance with standard ethical guidelines of KU Leuven and European Communities Guidelines on the Care and Use of Laboratory Animals (004-2014/EEC, 240-2013/EEC).

METHOD DETAILS

Rabies virus production

Rabies production method was similar to previously published methods [61,62]. Glycoprotein G-coated, G-deleted B19 rabies virus (G-coated SAD-ΔG-GCaMP6s RV) was amplified in B7GG cells, which express rabies glycoprotein G. For amplification, approximately 10^6 infectious units of G-coated SAD-ΔG-GCaMP6s RV were used to infect five 10-cm plates of 80% confluent B7GG cells followed by 2-6 hours of incubation. Then, infected B7GG cells were treated with 0.05% trypsin and split into twenty-five 10-cm plates. To harvest the virus, we collected the supernatant of the infected cells every 3 days. 5-6 harvests were performed. To concentrate the virus, the supernatant was firstly centrifuged at 2,500 RPM and filtered (VWR, 514-0027) to get rid of the cell debris. Then the virus was spun in an ultracentrifuge for 5-12 hours at 25,000 RPM and at 4°C. After ultracentrifugation, the supernatant was discarded and the pellet was dissolved in 200 µl of the original cell culture supernatant. The virus was tittered by counting a culture of infected BHK cells. To produce EnvA-coated SAD-ΔG-GCaMP6s RV, approximately 10^6 infectious units of G-coated SAD-ΔG-GCaMP6s RV were used to infect BHK-EnvA cells. The same procedure as for the G-coated RV amplification was then applied. EnvA-coated SAD-ΔG-GCaMP6s RV was tittered by infection of HEK293T-TVA cells. The titer used for injection ranged from 10^7 to 10^9 infectious units/ml (IU/ml).

Surgical procedures

Animals were quickly anesthetized with Isoflurane (Iso-vet 1000mg/ml) and then injected with a mixture of Ketamine and Medetomidine (0.75 mL Ketamine (100 mg/mL) + 1 mL Medetomidine (1 mg/mL) + 8.2 mL Saline). Mice were placed in a stereotaxic workstation (Narishige, SR-5N). Dura tear (NOVARTIS, 288/28062-7) was applied to protect the eyes. To label the ganglion cells in the parabigeminal nucleus circuit, we performed the surgery on wild type mice and injected herpes-simplex-virus (HSV, hEF1a-TVA950-T2A-rabiesG-IRES-mCherry, MIT viral core, RN714) and EnvA-coated SAD-ΔG-GCaMP6s RV. In our experiment, we used PV-Cre mice as wild type mice. For the first injection of HSV into the parabigeminal nucleus, we used micropipettes (Wiretrol® II capillary micropipettes, Drumond Scientific, 5-000-2005) with an open tip of 30 µm and an oil-based hydraulic micromanipulator MO-10 (Narishige) for stereotactic injections. Alternatively, we used an oil-based microinjector IM-9B (Narishige) with the corresponding micropipettes (Warner Instrument, G100-4) with

an open tip of 30 µm. The injection coordinates for a 4 weeks old mouse with a bregma-lambda distance of 4.7 mm were AP: -4.20; ML: ±1.95; DV: 3.50 mm. As the mice were different in body size, we adjusted the coordinates for each mouse according to their bregma-lambda distance. To label the injection sites, DiD (Thermo, D7757) was used to coat the pipette tip. We injected in total 100-400 nl HSV in single doses of up to 200 nl with a waiting time of 5-10 min after each injection. Twenty-one days later, we injected rabies virus (EnvA-coated SAD-ΔG-GCaMP6s) into the superior colliculus using the same method as for the HSV injections. The retinotopic location of the first injection into the parabigeminal nucleus or the pulvinar is unknown. To maximize the labelling of ganglion cells in the retina, we thus covered as much as possible of the superficial layer of the superior colliculus during the second injection. We injected 100-200 nl of rabies virus at a depth of 1.8 mm at 4 different locations within a 1 mm^2 field anterior of lambda and starting at the midline.

To label the pulvinar circuit, we performed the surgery on Ntsr1-GN209-Cre mice in combination with a conditional HSV (hEF1a-LS1L-TVA950-T2A-RabiesG-IRES-mCherry, MIT viral core, RN716) and EnvA-coated SAD-ΔG-GCaMP6s RV. The injection into pulvinar and superior colliculus were the same as described for the parabigeminal nucleus. The injection coordinates for the pulvinar in a 4 weeks old mouse with a bregma-lambda distance of 4.7 mm were AP: -1.85; ML: ±1.50; DV: 2.50 mm.

Following injection, the wound was closed using Vetbond tissue adhesive (3M,1469). After surgery, mice were allowed to recover on top of a heating pad and were provided with soft food and water containing antibiotics (emdotrim, ecuphar, BE-V235523).

Retina Immunohistochemistry

Mouse retinas were extracted eight days after the rabies virus injection into the superior colliculus. After anesthesia (120µl of Ketamine (100mg/ml) and Xylamine (2%) in saline per 20g body weight), eyes were gently touched with a soldering iron (Weller, BP650) to label the nasal part of the cornea and then enucleated. The retinas were extracted in 1x PBS (Diluted from 10x PBS (VWR, 437117K), pH 7.4). The dissected retinas were fixed in 4% paraformaldehyde (Histofix, ROTH, P087.5) for 30 min at 4 °C, and then transferred to a 24-well plate filled with 1x PBS and washed 3 times at room temperature or transferred into 15 ml 1x PBS and washed overnight or longer at 4 °C. After washing, retinas were transferred to wells containing 10% sucrose in 1x PBS with 0.1% NaN3 (w/v) and allowed to sink for 30 min at room temperature. Then retinas were transferred to wells containing 20% sucrose in 1x PBS with 0.1% NaN_3 (w/v) and allowed to sink for 1 hour at room temperature. Finally, retinas were put into 30% sucrose in 1x PBS with 0.1% NaN_3 (w/v) and allowed to sink overnight. The next day, freeze-cracking was performed: retinas were frozen on a slide fully covered with 30% sucrose for 3-5 min on dry ice. The slides were then thawed at room temperature. The freeze–thaw cycle was repeated two times. Retinas were washed 3 times for 10 min in 1x PBS, followed by incubation with blocking buffer (10% NDS, 1% BSA, 0.5% TritonX-100, 0.02% NaN_3 in 1x PBS) for at least 1 hour at room temperature. Primary antibody solution was added after blocking and retinas were incubated for 5-6 days under constant gentle shaking at room temperature. Primary antibodies were rabbit anti-GFP (Invitrogen, A-11122, 1:500) and goat anti-ChAT (Chemicon, Ab144P, 1:200). They were prepared in 3% NDS, 1% BSA, 0.5% TritonX-100, 0.02% NaN3 in 1x PBS. After incubation, retinas were washed 3 times for 10 min in 1x PBS with 0.5% TritonX-100 before being transferred into the secondary antibody solution (Alexa488 donkey anti-

rabbit (Invitrogen, A21206, 1/500) and Alexa633 donkey anti-goat (Invitrogen A-21082, 1:500); prepared in 3% NDS, 1% BSA, 0.5% TritonX-100, 0.02% NaN_3 in 1x PBS). Nuclei were stained with DAPI (Roche, 10236276001, 1:500) together with the secondary antibody solution. The retinas were incubated in the secondary antibody with DAPI solution overnight at 4 ℃. Slices were then washed 3 times in 1x PBS with 0.5% TritonX-100 and 1 time in 1x PBS. Before mounting, the water in the sample was exchanged with different concentrations of TDE (Sigma, 166782-500G) buffer (10% -> 25% -> 50% -> 97%) [63]. Then the retinas were embedded in ProLong® Gold Antifade Mountant (Thermo, P36934) and gently covered with a #0 coverslip (MARIENFEL, 0100032, No.0, 18*18 mm). To avoid squeezing the retinas, we put 4 strips of Parafilm (Parafilm, PM999) around the retina before adding the coverslip. Some of the retinas were mounted in 97% TDE with DABCO (Sigma, 290734) after increasing concentrations of TDE. Additionally, some retinas were mounted with ProLong® Gold Antifade Mountant directly after washing. Afterwards, nail polish was used to prevent evaporation and the samples were stored in darkness at 4 ℃.

Retina Immunohistochemistry (for RGC molecular marker staining)

Similar procedures were used to stain the retinas for neurofilament or CART. After fixation, freeze-cracking and blocking, primary antibody solution was added and the retinas were incubated for 5-6 days with gentle shaking at room temperature. Primary antibodies used were chicken anti-GFP (Invitrogen, A-10262, 1:500), goat anti-ChAT (Chemicon, Ab144P, 1:200), mouse SMI32 (Biolend, 801701,1:1000) and rabbit anti-CART (Phoenix, H-003-62,1/500). They were prepared in 3% NDS, 1% BSA, 0.5% TritonX-100, 0.02% NaN_3 in 1x PBS. Retinas were washed 3 times for 15 min in 1x PBS with 0.5% TritonX-100 before being transferred into the secondary antibody solution consisting of Alexa488 donkey anti-chicken (ImmunoJackson, 703-545-155, 1:500) and Alexa633 donkey anti-goat (Invitrogen A-21082, 1:500), Cy3 donkey anti-mouse (ImmunoJackson, 715-165-151, 1:400) and DyLight™ 405 donkey anti-rabbit (ImmunoJackson, 715-475-150, 1:200) with 3% NDS, 1% BSA, 0.5% TritonX-100, 0.02% NaN_3 in 1x PBS. Retinas were incubated in secondary antibody solution overnight at 4℃. Slices were washed 3 times for 10-15min in 1x PBS with 0.5% TritonX-100 and 1 time in 1x PBS. After washing, the retinas were immersed in different concentrations of TDE buffer, then were mounted with either 97% TDE with DABCO or ProLong® Gold Antifade Mountant. Some of the retinas were directly mounted with ProLong® Gold Antifade Mountant without increasing concentrations of TDE.

Brain Immunohistochemistry

After removing the eyes, mice were immediately perfused with 1x PBS and 4% paraformaldehyde (PFA) and brains were post-fixed in 4% PFA overnight at 4 ℃. Vibratome sections (100 μm) were collected in 1x PBS and were incubated in blocking buffer (1x PBS + 0.3% Triton X-100 + 3% Donkey serum) at room temperature for 1 hour. Then slices were incubated with primary antibodies in blocking buffer overnight at 4 ℃. The next day, slices were washed 3 times for 10 min in 1x PBS with 0.3% TritonX-100 and incubated in secondary antibody solution diluted in blocking buffer for 2 hours at room temperature or overnight at 4 ℃. Primary antibodies used were rabbit anti-GFP (Thermo Fisher, A-11122, 1:500) and chicken anti-mCherry (Novus, NBP2-25158, 1:1000) and secondary antibodies used were Alexa488 donkey anti-rabbit (Thermo Fisher, A21206, 1:500-1000) and Cy3 donkey anti-chicken (ImmunoJackson,

703-166-155, 1:800-1000). Sections were then again washed 3 times for 10 min in 1x PBS with 0.3% TritonX-100 and 1 time in 1x PBS, covered with mounting medium (Dako, C0563) and a glass coverslip.

Confocal Microscopy

Confocal microscopy was performed on a Zeiss LSM 710 microscope. Overview images of the retina and brain were obtained with a 10x (plan-APOCHROMAT 0.45 NA, Zeiss) objective. The following settings were used: zoom 0.7, 4x4-tiles with 0 to 15% overlap, 2.37 µm/pixel resolution. For single retina ganglion cell scannings, we used a 63x (plan-APOCHROMAT 1.4 NA, Zeiss) objective. The following settings were used: zoom 0.7, 2x2-tiles or more (depending on size and number of cells) with 0 to 15% overlap. This resulted in an XY-resolution of 0.38 µm/pixel and a Z-resolution between 0.25 and 0.35 µm/pixel. The Z-stacks covered approximately 50 µm in depth.

QUANTIFICATION AND STATISTICAL ANALYSIS

Morphology of individual ganglion cells

The confocal Z-stacks were down-sampled and thresholded. The position of the ChAT-planes was extracted and used to warp both the ChAT-signal as well as the binary Z-stack of the labelled cell. Then, dendrites from other cells, noise, and axons were removed and the position of the cell body was measured. The resulting warped dendritic tree was used for further analysis such as computation of the dendritic profile and area measurements. All scripts can be found on github (https://github.com/farrowlab/).

Down-sampling and binarization: The confocal Z-stacks of individual ganglion cells were denoised using the CANDLE package for MATLAB [64] and down-sampled to have a resolution of XYZ = 0.5 x 0.5 x (0.25 to 0.35) µm per pixel and saved as MATLAB files. We then manually selected a threshold to transform the GFP-signal (i.e. the labelled cell) into a binary version where the whole dendritic tree was visible but noise was reduced as much as possible using an adapted version of the method described in [33,34].

Extraction of ChAT-positions: ChAT-band positions were either extracted manually or automatically using a convolutional neural network. For manual extraction, the ChAT-signal was smoothed using a two-dimensional standard-deviation filtering approach in the XY plane with a size of 21 x 21 pixels. The resulting Z-stacks were loaded into Fiji [65]. ChAT-band positions were marked as described in [33]. Briefly, we labelled points in the ON- and OFF-band with an approximate spacing of 20 µm in X- and Y-direction. For automated labelling, an end-to-end 3D Convolutional Neural Network called V-Net with a Dice Loss Layer [66] was trained on noisy greyscale images of ChAT-images, to denoise and remove any cell bodies, creating a probability map of background and foreground, with foreground being voxels that might belong to the ChAT-bands. Two smoothness-regularized-least squares surfaces were fitted to manually labelled data to train the algorithm and to create ground truth binary masks. Then, Otsu's thresholding method combined with connected component analysis was performed on the resulting probability map to automatically locate the points that belong to the ChAT-bands in new data-sets. Finally, two surfaces were independently fit to the corresponding data points to approximate the two ChAT-bands (https://github.com/farrowlab/ChATbandsDetection).

Warping: An adapted version of the code published in Sumbul et al. 2014a was used to warp the GFP-signal. Briefly, the ChAT-band locations were used to create a surface map, which then was straightened in 3D-space. Then, the thresholded and binarized GFP-signal was warped accordingly.

Soma position and removal of noise: After warping, the soma position was determined by filtering the GFP-signal with a circular kernel (adapted from [33]). If this method detected the soma, it was used to remove the soma from the GFP-data and the center of mass was taken as the soma position. If this automated metod failed, the soma position was marked manually. Afterwards, dendrites of other cells, axons, and noise were removed manually: The warped GFP-signal was plotted in side-view and en-face view in MATLAB and pixels belonging to the cell were circled manually.

Computation of the dendritic profile and area: The distribution of the cell's dendritic tree was computed as described in Sumbul et al. 2014a. Briefly, the Z-positions of all GFP-positive pixels were normalized to be between -0.5 and 0.5. Then the Fourier transform of an interpolating low-pass filter was used to filter the Z-positions. This resulted in a vector containing the distribution of pixels in the Z-direction. If necessary, this profile was used to manually remove remaining axonal or somal pixels. In this case, the dendritic profile was computed again after cleaning of the data. The area of the dendritic tree was approximated by computing a convex hull (regionprops function in MATLAB). When diameters are given, they were calculated as $D = 2*(\text{area} / \pi)^{1/2}$.

Down-sampling of dendritic tree for plotting: For en-face plots of the dendritic arbor, they were down-sampled by calculating the local neighborhood median of all labelled pixels in patches of 50 x 50 pixels and with a sliding window of 10 pixels.

Clustering of retinal ganglion cell morphology

Affinity-propagation clustering: The dendritic stratification profiles of 301 ganglion cells were smoothed with the MATLAB function movmean (moving average with sliding window of 5 data points corresponding to 1.7 a.u. in stratification depth). The profiles of manually identified bistratified cells were set to negative values. The median dendritic profile of cells for which the molecular identity was known (SMI32 or CART), was calculated (4 different SMI32 cell types, 1 CART). Then the 5 first principle components of those medians and of the dendritic profiles of cells without known molecular identity were computed using sparse PCA (http://www2.imm.dtu.dk/projects/spasm/) and the similarity matrix of these principle components was calculated using the pdist function of MATLAB using Euclidean distance. Affinity-propagation (apcluster function in MATLAB) was used to cluster the similarity matrix with different preference values ranging from –1 to 0.6. The preference value for the 5 cluster centers based on SMI32- and CART-positive cells was always set to 1. Cells with known molecular identity were assigned to the clusters to whose median they contributed. Three validation indices (Calinski-Harabasz, Silhouette, Davies-Bouldin) were computed using the evalclusters function in MATLAB, normalized, and their median was used to determine the optimal preference value.

tSNE visualization: For visualization of the clustering result, we generated a five-dimensional non-linear embedding of the cells using t-distributed Stochastic Neighbor Embedding, tSNE[45]. We used the smoothed dendritic profiles as input data, used cosine as a distance measurement, and set the number of

PCA dimensions, which are calculated in a first step, to 25. For the graph in this paper, we show comparisons of the resulting tSNE dimension 1, 2, and 4.

Size distribution analysis

Comparison to PV cells: For size distribution comparisons, we used previously published data from 8 different types of parvalbumin-positive (PV) ganglion cells [47]. For each of our 12 clusters, we looked for a PV-type with a similar stratification depth and average dendritic field size. If there was such a PV-type, we calculated the median and quartiles of the dendritic field diameters of all cells of this type and compared it to our data.

Retinotopic size distribution: For retinotopic size distribution calculations, we computed a moving median diameter within a circular window of 250 µm radius, moving by 100 µm. The resulting 50 x 50 median size matrix was convolved with a gaussian with sigma = 200 µm (using MATLAB function fspecial and nanconv).

Quantification of SMI32+ cells and CART+ cells

Numbers of double-labelled cells: To quantify the number of double-positive cells for CART/GCaMP6s and SMI32/GCaMP6s, we scanned a z-stack (1 to 5 µm Z-resolution) of the whole retina using the confocal microscope with an 10x objective. Images of the anti-CART or SMI32 and the anti-GFP staining were opened in Fiji. For counting $CART^+$ cells, cells were marked using the point tool and counted manually. Note that the anti-CART antibody also labels a group of amacrine cells, therefore the complete Z-stack should be checked for each $CART^+$ cell to make sure that the labelling truly overlaps with the anti-GFP signal. The CART expression pattern was consistent with previous reports [67]. In total we counted 3 retinas for parabigeminal experiments and 6 retinas for pulvinar experiments. For counting $SMI32^+$ cells, cells were counted manually using the cell counter plugin. In total we counted 3 retinas for parabigeminal experiments and 4 retinas for pulvinar experiments.

Numbers of cells for types of alpha cells: To test which of the four alpha cell types were part of each circuit, we acquired small high-resolution Z-stacks (2.5 µm/pixel) of XY = 103 x 103 µm size (128 x 128 pixel, 63x objective) covering the full depth of the dendritic tree and centered around the soma of 91 $SMI32^+$ / $GCaMP6s^+$ cells in n = 3 retinas from parabigeminal experiments and 90 $SMI32^+$ / $GCaMP6s^+$ cells in n = 3 retinas from pulvinar experiments. We plotted top and side views of each Z-stack in MATLAB and manually decided for each cell if it was a sustained ON-alpha cell (dendrites below the ON- ChAT band), a transient ON-alpha (dendrites just above the ON- ChAT band), a transient OFF-alpha (dendrites just below or on the OFF- ChAT band) or a sustained OFF-alpha cell (dendrites above the OFF- ChAT band).

Statistics

Dendritic tree size: To compare dendritic tree diameter distributions, we applied the Kolmogorov-Smirnov test (kstest2 function in MATLAB). Medians were compared by the Wilcoxon Ranksum test (ranksum function in MATLAB). We used both Pearson correlation and Spearman correlation (corr function in MATLAB) to test for significant gradients in the retinotopic distribution of dendritic tree diameters.

References

1. Zeng, H. & Sanes, J. R. Neuronal cell-type classification: Challenges, opportunities and the path forward. *Nat. Rev. Neurosci.* **18,** 530–546 (2017).

2. Lorente de No, R. Vestibulo–ocular-reflex arc. *Arch. Neurol. Psychiatry Chicago* **30,** 245–291 (1933).

3. Chen, S.-K., Badea, T. C. & Hattar, S. Photoentrainment and pupillary light reflex are mediated by distinct populations of ipRGCs. *Nature* **476,** 92–5 (2011).

4. Lundberg, A. Multisensory Control of Spinal Reflex Pathways. *Prog. Brain Res.* **50,** 11–28 (1979).

5. Rose, T., Jaepel, J., Hübener, M. & Bonhoeffer, T. Cell-specific restoration of stimulus preference after monocular deprivation in the visual cortex. *Science (80-.).* **352,** 1319–1322 (2016).

6. Dhawale, A. K., Smith, M. A. & Ölveczky, B. P. The Role of Variability in Motor Learning. *Annu. Rev. Neurosci.* **40,** 479–498 (2017).

7. Aponte, Y., Atasoy, D. & Sternson, S. M. AGRP neurons are sufficient to orchestrate feeding behavior rapidly and without training. *Nat. Neurosci.* **14,** 351 (2011).

8. Gandhi, N. J. & Katnani, H. A. Motor functions of the superior colliculus. *Annu. Rev. Neurosci.* **34,** 205–31 (2011).

9. Hong, W., Kim, D.-W. & Anderson, D. J. Antagonistic Control of Social versus Repetitive Self-Grooming Behaviors by Separable Amygdala Neuronal Subsets. *Cell* **158,** 1348–1361 (2018).

10. Tinbergen, N. *The study of instinct*. (Clarendon Press, 1951).

11. Morgan, J. L. *et al.* Article The Fuzzy Logic of Network Connectivity in Mouse Visual Thalamus. *Cell* **165,** 192–206 (2016).

12. Cruz-Martín, A. *et al.* A dedicated circuit links direction-selective retinal ganglion cells to the primary visual cortex. *Nature* **507,** 358–61 (2014).

13. Rompani, S. B. *et al.* Different Modes of Visual Integration in the Lateral Geniculate Nucleus Revealed by Single-Cell-Initiated Transsynaptic Tracing. *Neuron* **93,** 767–776 (2017).

14. Glickfeld, L. L., Andermann, M. L., Bonin, V. & Reid, R. C. Cortico-cortical projections in mouse visual cortex are functionally target specific. *Nat. Neurosci.* **16,** 219 (2013).

15. Gale, S. D. & Murphy, G. J. Distinct representation and distribution of visual information by specific cell types in mouse superficial superior colliculus. *J. Neurosci.* **34,** 13458–71 (2014).

16. Ellis, E. M., Gauvain, G., Sivyer, B. & Murphy, G. J. Shared and distinct retinal input to the mouse superior colliculus and dorsal lateral geniculate nucleus. *J. Neurophysiol.* **116,** 602–610 (2016).

17. Baden, T. *et al.* The functional diversity of retinal ganglion cells in the mouse. *Nature* **529,** 345–50 (2016).

18. Sanes, J. R. & Masland, R. H. The Types of Retinal Ganglion Cells: Current Status and Implications for Neuronal Classification. *Annu. Rev. Neurosci.* **38,** 221–246 (2014).

19. Dhande, O. S., Stafford, B. K., Lim, J.-H. A. & Huberman, A. D. Contributions of Retinal Ganglion Cells to Subcortical Visual Processing and Behaviors. *Annu. Rev. Vis. Sci.* **1,** 291–328 (2015).

20. Martersteck, E. M. *et al.* Diverse Central Projection Patterns of Retinal Ganglion Cells. *Cell Rep.* **18,** 2058–2072 (2017).

21. Farrow, K. & Masland, R. H. Physiological clustering of visual channels in the mouse retina. *J. Neurophysiol.* **105,** 1516–30 (2011).

22. Roska, B. & Werblin, F. Vertical interactions across ten parallel, stacked representations in the mammalian retina. *Nature* **410,** 583–587 (2001).

23. Linden, R. & Perry, V. H. Massive retinotectal projection in rats. *Brain Res.* **272,** 145–149 (1983).

24. Vaney, D. I., Peichl, L., Wässle, H. & Illing, R. B. Almost all ganglion cells in the rabbit retina project to the superior colliculus. *Brain Res.* **212,** 447–453 (1981).

25. Hofbauer, A. & Dräger, U. C. Depth segregation of retinal ganglion cells projecting to mouse superior colliculus. *J. Comp. Neurol.* **234,** 465–474 (1985).

26. Shang, C. *et al.* A parvalbumin-positive excitatory visual pathway to trigger fear responses in mice. *Science (80-.).* **348,** 1472–1477 (2015).

27. Wei, P. *et al.* Processing of visually evoked innate fear by a non-canonical thalamic pathway. *Nat. Commun.* **6,** 6756 (2015).

28. Hong, Y. K., Kim, I. J. & Sanes, J. R. Stereotyped axonal arbors of retinal ganglion cell subsets in the mouse superior colliculus. *J. Comp. Neurol.* **519,** 1691–1711 (2011).

29. Kim, I.-J., Zhang, Y., Meister, M. & Sanes, J. R. Laminar Restriction of Retinal Ganglion Cell Dendrites and Axons: Subtype-Specific Developmental Patterns Revealed with Transgenic Markers. *J. Neurosci.* **30,** 1452–1462 (2010).

30. May, P. J. The mammalian superior colliculus: Laminar structure and connections. *Prog. Brain Res.* **151,** 321–378 (2005).

31. Chandrasekaran, A. R., Shah, R. D. & Crair, M. C. Developmental Homeostasis of Mouse Retinocollicular Synapses. *J. Neurosci.* **27,** 1746–1755 (2007).

32. Shi, X. *et al.* Retinal origin of direction selectivity in the superior colliculus. *Nat. Neurosci.* **20,** 550–558 (2017).

33. Sümbül, U. *et al.* A genetic and computational approach to structurally classify neuronal types. *Nat. Commun.* **5,** 3512 (2014).

34. Sumbul, U., Zlateski, A., Vishwanathan, A., Masland, R. H. & Seung, H. S. Automated computation of arbor densities: a step toward identifying neuronal cell types. *Front. Neuroanat.* **8,** 139 (2014).

35. Coombs, J., van der List, D., Wang, G. Y. & Chalupa, L. M. Morphological properties of mouse retinal ganglion cells. *Neuroscience* **140,** 123–136 (2006).

36. Kong, J. H., Fish, D. R., Rockhill, R. L. & Masland, R. H. Diversity of ganglion cells in the mouse

retina: Unsupervised morphological classification and its limits. *J. Comp. Neurol.* **489,** 293–310 (2005).

37. Sun, W., Li, N. & He, S. Large-scale morphological survey of mouse retinal ganglion cells. *J. Comp. Neurol.* **451,** 115–126 (2002).

38. Badea, T. C. & Nathans, J. Quantitative analysis of neuronal morphologies in the mouse retina visualized by using a genetically directed reporter. *J. Comp. Neurol.* **480,** 331–351 (2004).

39. Bleckert, A., Schwartz, G. W., Turner, M. H., Rieke, F. & Wong, R. O. L. Visual space is represented by nonmatching topographies of distinct mouse retinal ganglion cell types. *Curr. Biol.* **24,** 310–315 (2014).

40. Krieger, B., Qiao, M., Rousso, D. L., Sanes, J. R. & Meister, M. Four alpha ganglion cell types in mouse retina: Function, structure, and molecular signatures. *PLoS One* **12,** 1–21 (2017).

41. Peichl, L., Ott, H. & Boycott, B. B. Alpha ganglion cells in mammalian rentinae. *Proc. R. Soc. Lond. B Biol Sci.* **231,** (1987).

42. Huberman, A. D. *et al.* Architecture and Activity-Mediated Refinement of Axonal Projections from a Mosaic of Genetically Identified Retinal Ganglion Cells. *Neuron* **59,** 425–438 (2008).

43. Dhande, O. S. *et al.* Genetic dissection of retinal inputs to brainstem nuclei controlling image stabilization. *J. Neurosci.* **33,** 17797–813 (2013).

44. Frey, B. J. & Dueck, D. Clustering by passing messages between data points. *Science* **315,** 972–976 (2007).

45. Van Der Maaten, L. J. P. & Hinton, G. E. Visualizing high-dimensional data using t-sne. *J. Mach. Learn. Res.* **9,** 2579–2605 (2008).

46. Münch, T. a *et al.* Approach sensitivity in the retina processed by a multifunctional neural circuit. *Nat. Neurosci.* **12,** 1308–1316 (2009).

47. Farrow, K. *et al.* Ambient illumination toggles a neuronal circuit switch in the retina and visual perception at cone threshold. *Neuron* **78,** 325–338 (2013).

48. Jeon, C. J., Strettoi, E. & Masland, R. H. The major cell populations of the mouse retina. *J Neurosci* **18,** 8936–8946 (1998).

49. Drager, U. C. & Olsen, J. F. Ganglion cell distribution in the retina of the mouse. *Investig. Ophthalmol. Vis. Sci.* **20,** 285–293 (1981).

50. Nath, A. & Schwartz, G. W. Cardinal Orientation Selectivity Is Represented by Two Distinct Ganglion Cell Types in Mouse Retina. *J. Neurosci.* **36,** 3208–21 (2016).

51. Zhang, Y., Kim, I.-J., Sanes, J. R. & Meister, M. The most numerous ganglion cell type of the mouse retina is a selective feature detector. *Proc. Natl. Acad. Sci. U. S. A.* **109,** E2391-8 (2012).

52. Nath, A. & Schwartz, G. W. Electrical synapses convey orientation selectivity in the mouse retina. *Nat. Commun.* **8,** 2025 (2017).

53. Volgyi, B., Chheda, S. & Bloomfield, S. A. Tracer coupling patterns of the ganglion cell subtypes in the mouse retina. *J. Comp. Neurol.* **512,** 664–687 (2009).

54. Pang, J.-J., Gao, F. & Wu, S. M. Light-evoked excitatory and inhibitory synaptic inputs to ON and OFF alpha ganglion cells in the mouse retina. *J. Neurosci.* **23,** 6063–6073 (2003).

55. Gale, S. D. & Murphy, G. J. Active Dendritic Properties and Local Inhibitory Input Enable Selectivity for Object Motion in Mouse Superior Colliculus Neurons. *J. Neurosci.* **36,** 9111–23 (2016).

56. Callaway, E. M. & Luo, L. Monosynaptic Circuit Tracing with Glycoprotein-Deleted Rabies Viruses. *J. Neurosci.* **35,** 8979–8985 (2015).

57. Hammer, S., Monavarfeshani, A., Lemon, T., Su, J. & Fox, M. A. Multiple Retinal Axons Converge onto Relay Cells in the Adult Mouse Thalamus. *Cell Rep.* **12,** 1575–1583 (2015).

58. Han, Y. *et al.* A single-cell anatomical blueprint for intracortical information transfer from primary visual cortex. *bioRxiv* 148031 (2017). doi:10.1101/148031

59. Hippenmeyer, S. *et al.* A developmental switch in the response of DRG neurons to ETS transcription factor signaling. *PLoS Biol.* **3,** e159 (2005).

60. Madisen, L. *et al.* A robust and high-throughput Cre reporting and characterization system for the whole mouse brain. *Nat. Neurosci.* **13,** 133–140 (2010).

61. Osakada, F. & Callaway, E. M. Design and generation of recombinant rabies virus vectors. *Nat. Protoc.* **8,** 1583–1601 (2013).

62. Yonehara, K. *et al.* The first stage of cardinal direction selectivity is localized to the dendrites of retinal ganglion cells. *Neuron* **79,** 1078–1085 (2013).

63. Staudt, T., Lang, M. C., Medda, R., Engelhardt, J. & Hell, S. W. 2,2'-thiodiethanol: a new water soluble mounting medium for high resolution optical microscopy. *Microsc. Res. Tech.* **70,** 1–9 (2007).

64. Coupé, P., Munz, M., Manjón, J. V, Ruthazer, E. S. & Louis Collins, D. A CANDLE for a deeper in vivo insight. *Med. Image Anal.* **16,** 849–864 (2012).

65. Schindelin, J. *et al.* Fiji: An open-source platform for biological-image analysis. *Nat. Methods* **9,** 676–682 (2012).

66. Milletari, F., Navan, N. & Ahmadi, S.-A. V-Net: Fully Convolutional Neural Networks for Volumetric Medical Image Segmentation. *arXiv* (2016).

67. Kay, J. N. *et al.* Retinal Ganglion Cells with Distinct Directional Preferences Differ in Molecular Identity, Structure, and Central Projections. *J. Neurosci.* **31,** 7753–7762 (2011).

Supplementary Information

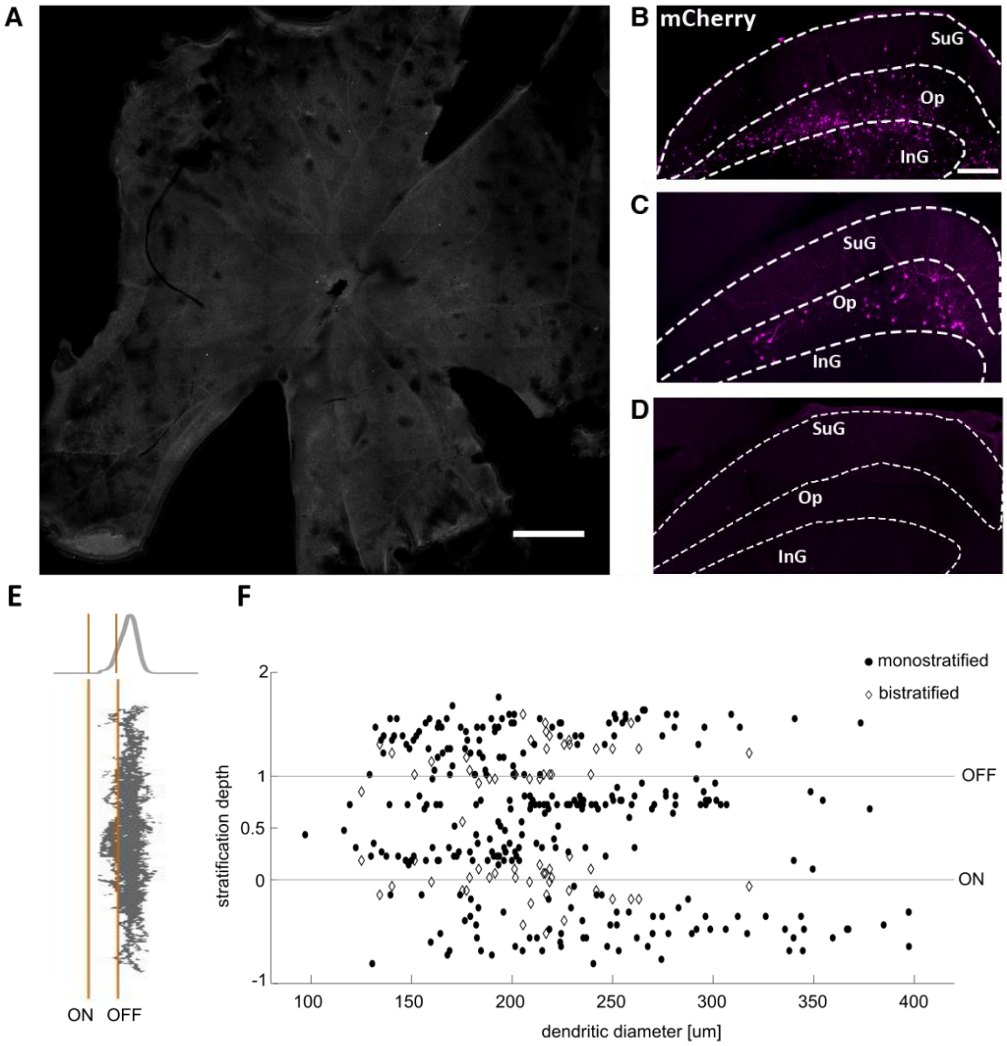

Supplemental Figure 1: Viral tracing with EnvA-coated rabies virus and herpes-simplex-virus (HSV). A) The whole-mount retina stained with antibody for GCamp6s after EnvA-coated SAD-ΔG-GCaMP6s rabies virus injection to superior colliculus alone without first injection of HSV. No labelled cells are observed after 11 days injection. Scale bar: 500μm. **B)** Injection of non-conditional HSV to parabigeminal nuclei labelled superior colliculus neurons. Neurons were stained with anti-mCherry antibody, showed in magenta. **C)** Injection of conditional HSV to pulvinar labelled superior colliculus neurons. Neurons were stained with anti-mCherry antibody, showed in magenta. **D)** Injection of conditional HSV to wild-type mouse. Quite few labelled cells are observed after 21 days injection. Scale bar = 200μm. **E)** The distribution of the dendritic tree in depth was summed to create a stratification profile (F) Stratification depth and dendritic tree diameter of all 301 labelled retinal ganglion cells from both experimental conditions.

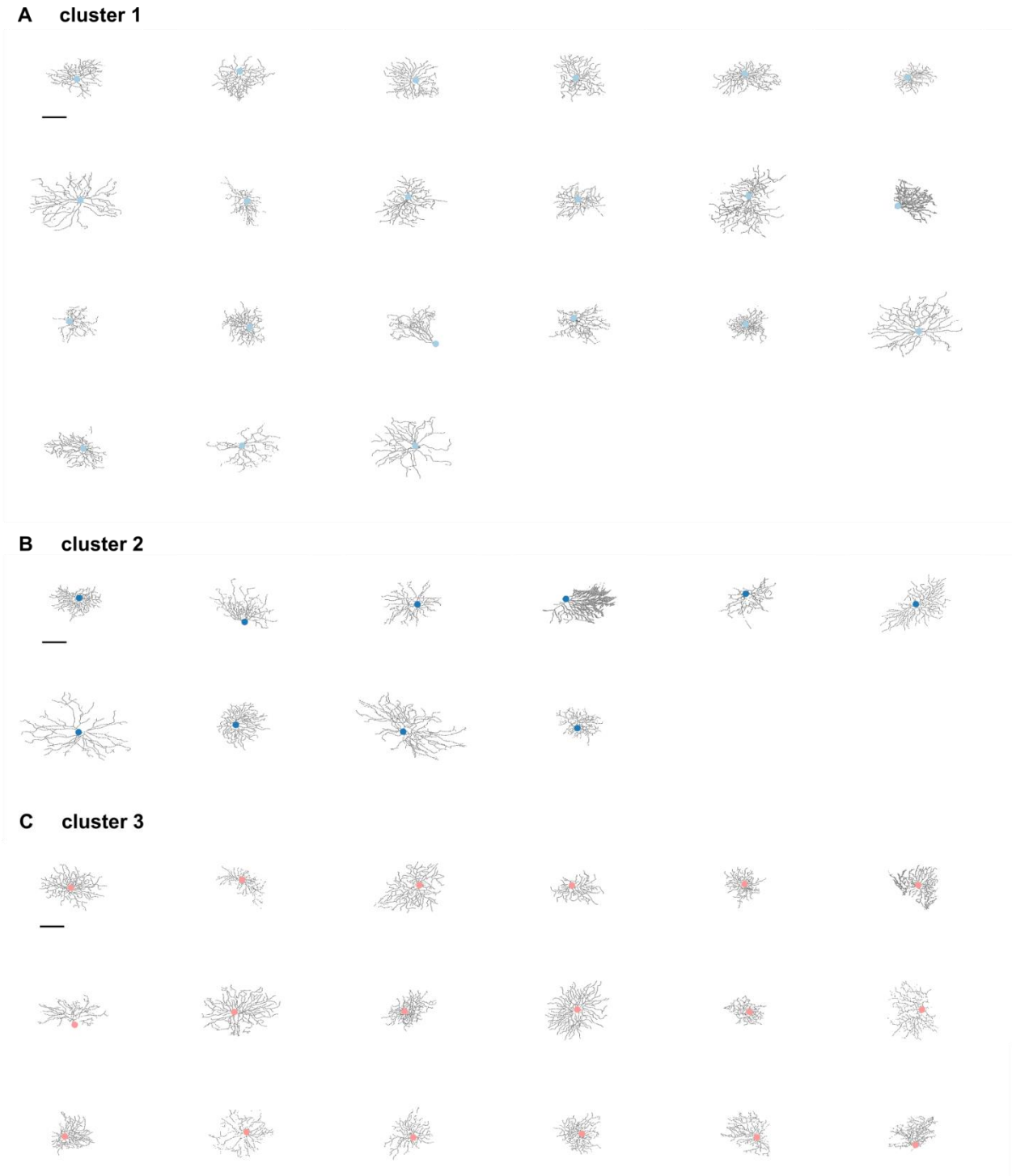
A cluster 1
B cluster 2
C cluster 3

D cluster 4

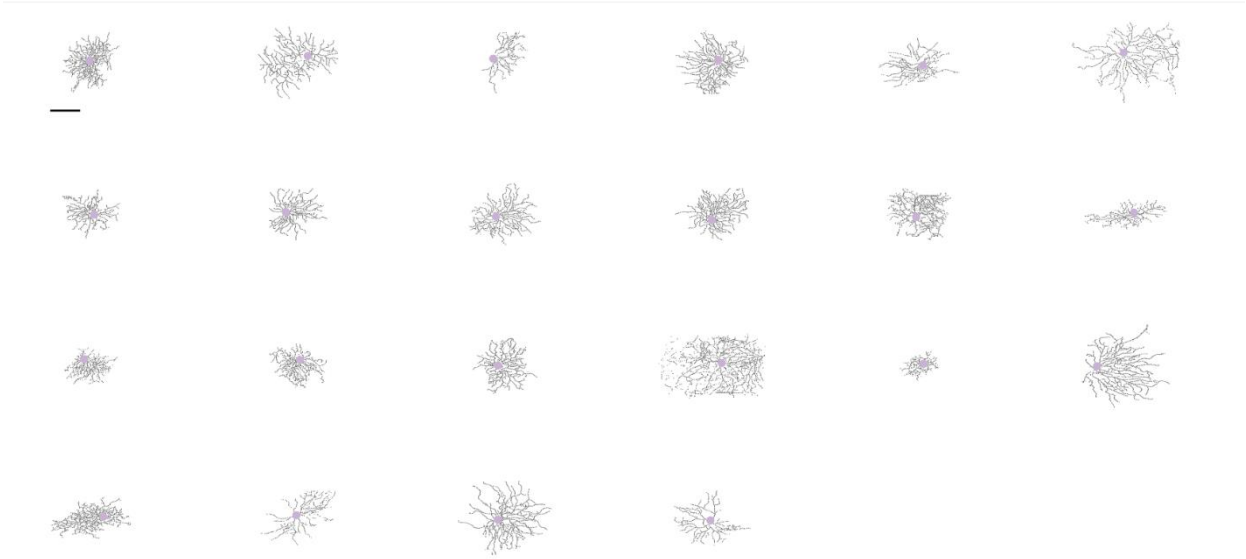

E cluster 5

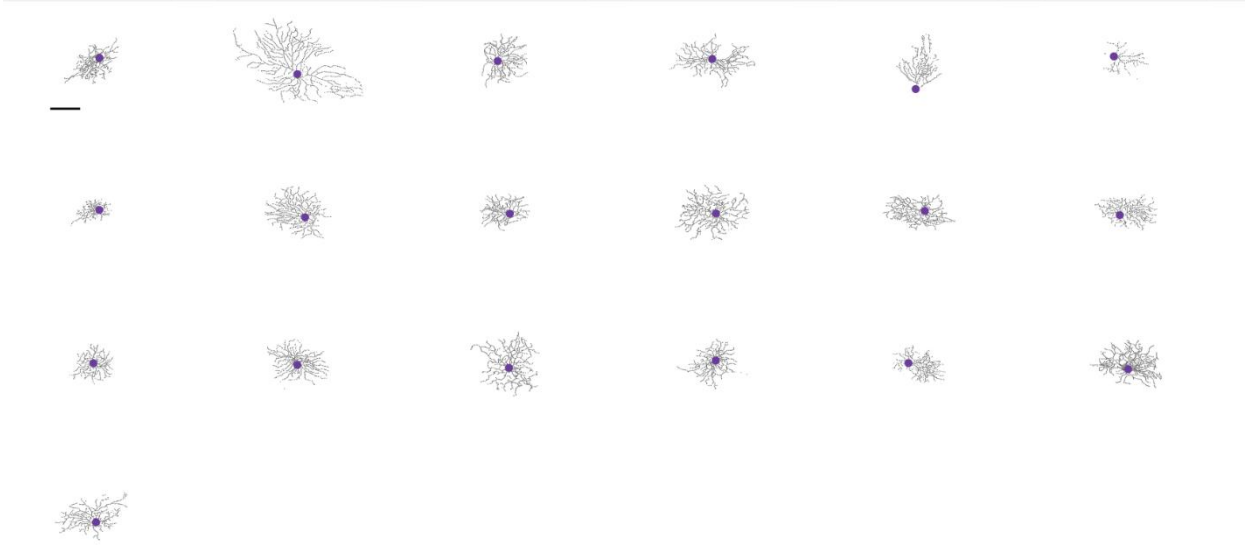

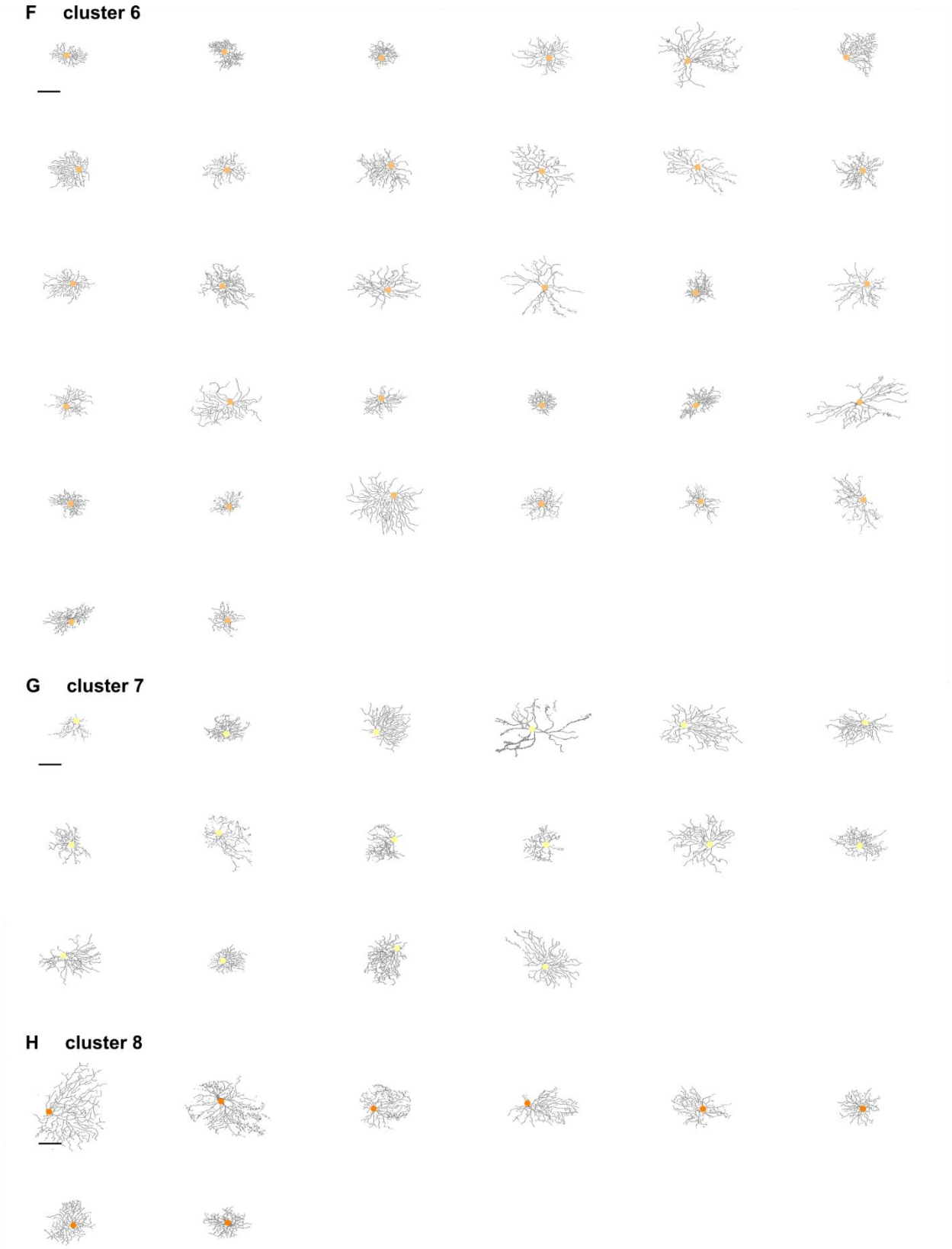
F cluster 6
G cluster 7
H cluster 8

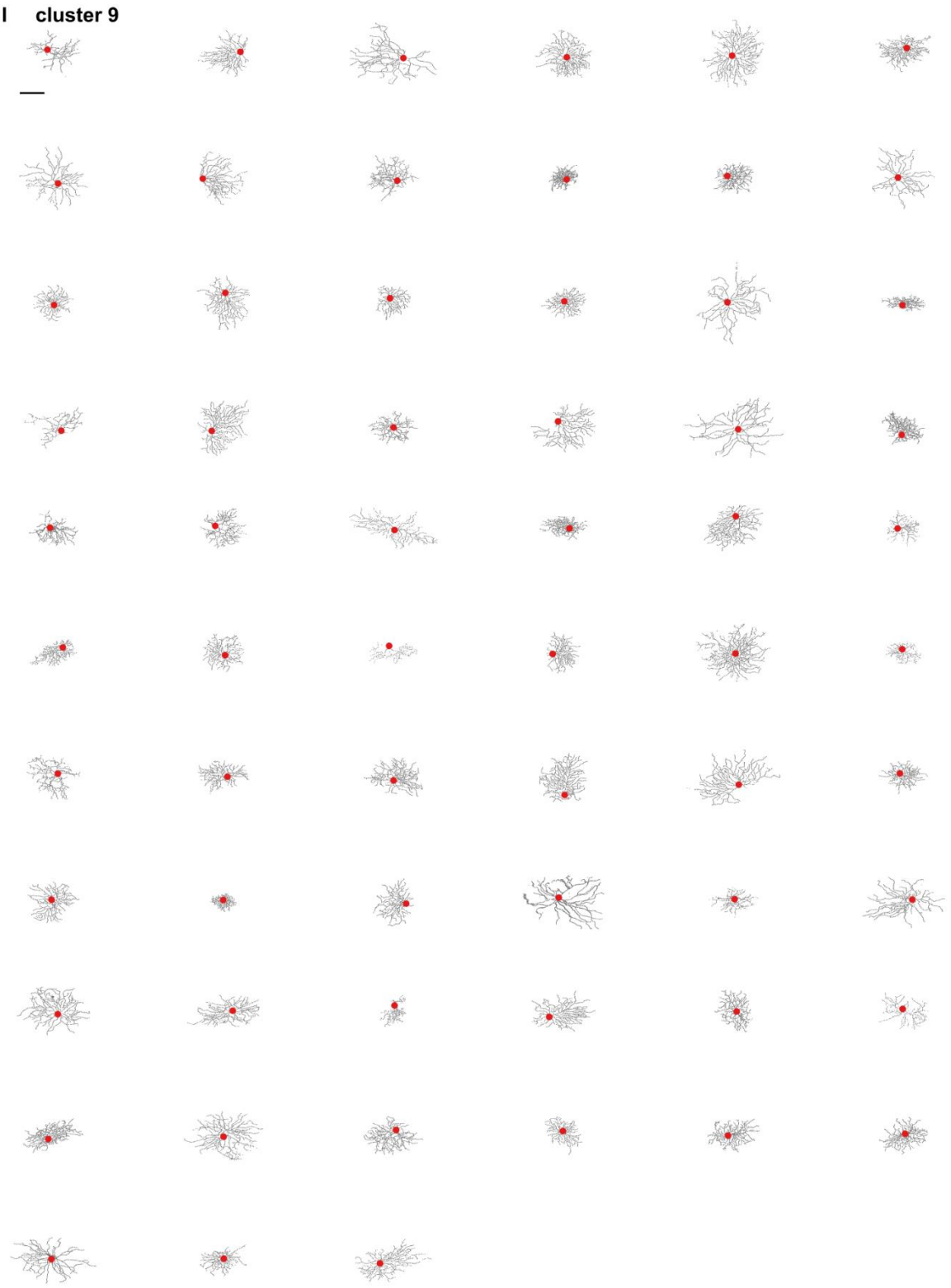
I cluster 9

J cluster 10

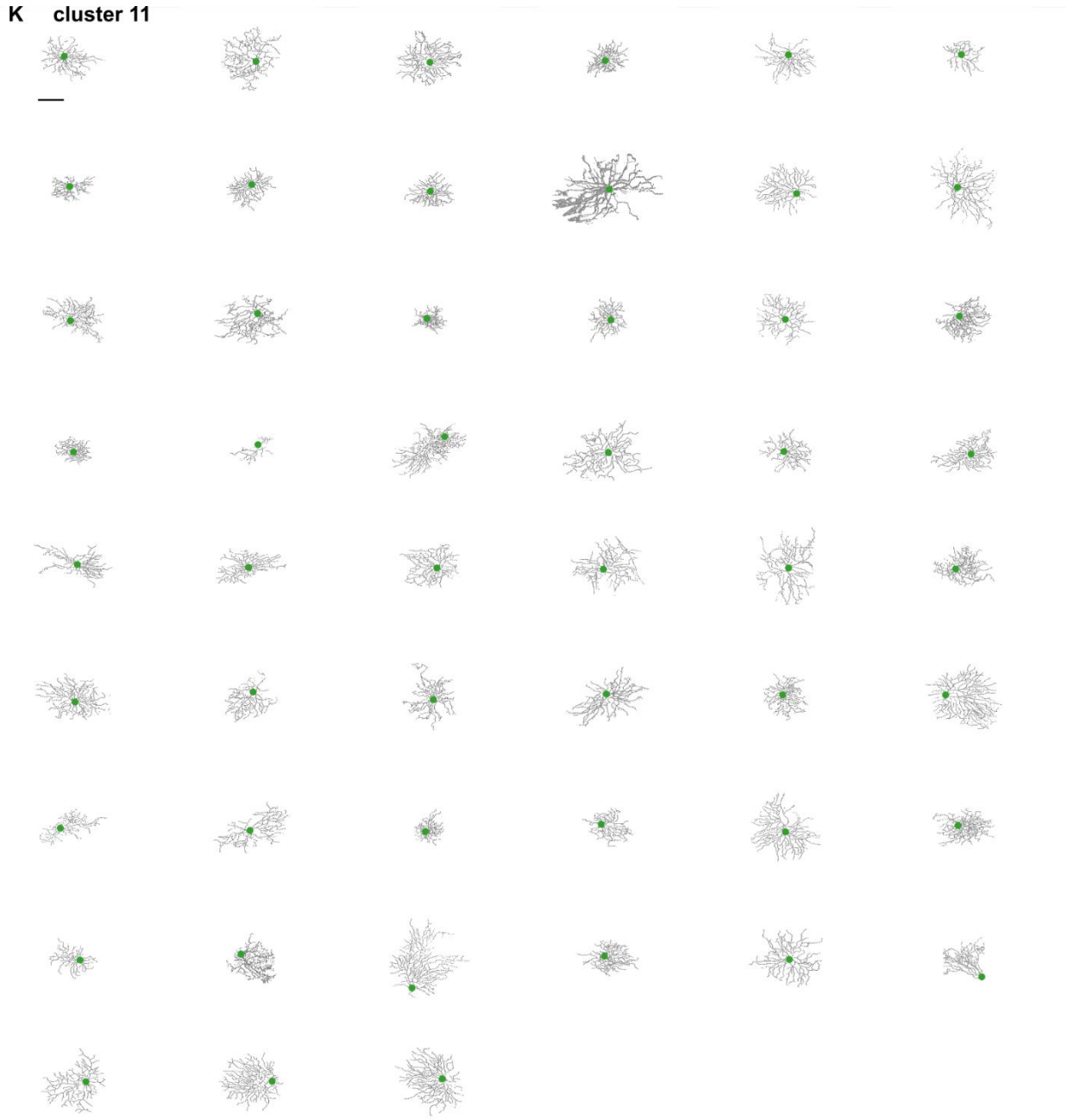
K cluster 11

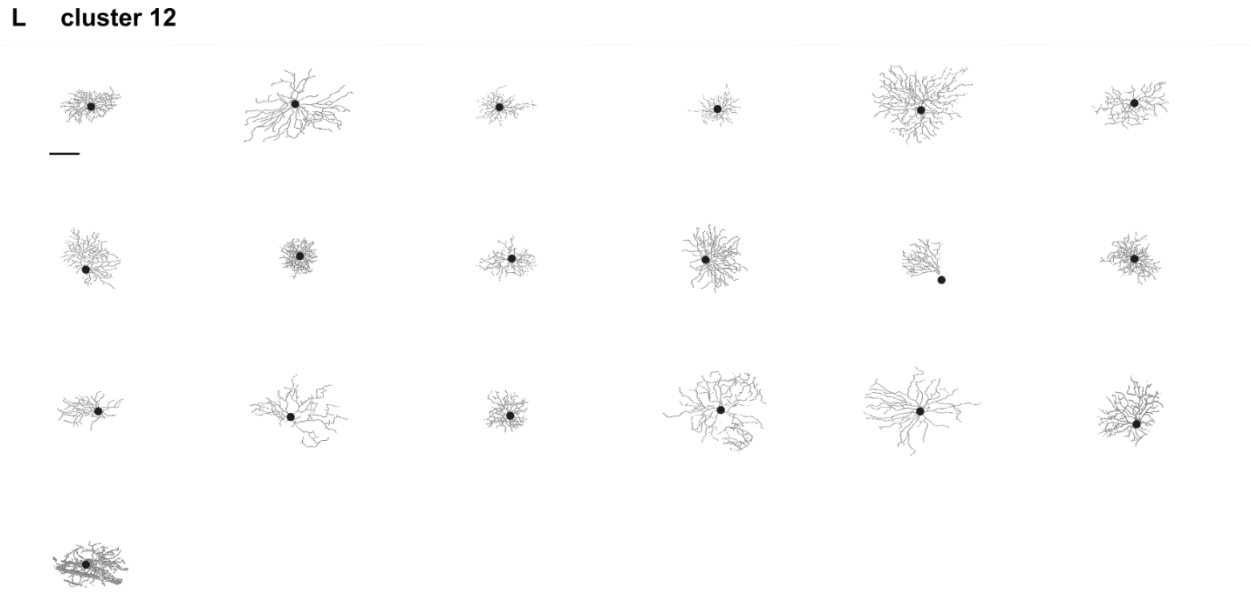

Supplemental Figure 2: All 301 cells in their corresponding cluster. Cells are sorted by their similarity to the cluster center (from closest do most distant). Scale bar: 100 µm.

		Parabigeminal nucleus						Shared			Pulvinar		
		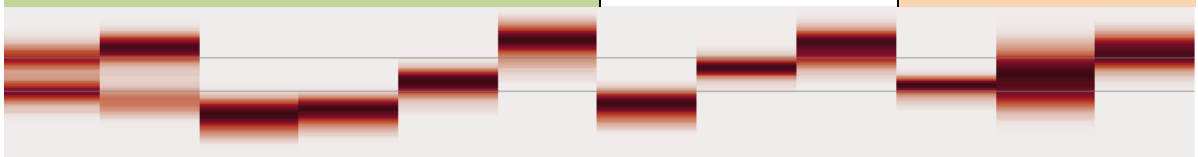											
Cluster #		1	2	3	4	7	12	5	9	11	6	8	10
Molecular Marker		CART			SMI32				SMI32	SMI32	SMI32		
Putative types	Baden et al. 2016	**DS1 (12)**	ON-DS2 (26)	Suppr. by contrast ON (28)	**sONa (24)**		OFF step (3)		**tOFFa (8)**	**sOFFa (5)**	trans fast ON (18-20)	**ON-OFF local OS (14)**	slow-OFF (4)
	Sümbül et al. 2014	**D (ONOFF-DS, BDa)**	V	**C (Kb)**		X	**Z**	**U**	**F (tOFFa, CB2)**		**X**	**E (W3, BDb)**	
	Dhande et al. 2015	**ONOFF-DS**	M3	M2	**sONa**		W7B	ON-DS	**tOFFa, W7A**	**W7B**		**W3**	
	Farrow et al. 2013	**PV0 (ONOFF-DS)**			**PV1 (sONa)**				**PV5 (tOFFa)**	**PV6 (sOFFa)**	**PV2**	**PV3 (W3)**	
	Nath & Schwartz 2016		**ON-vOS**										
	Völgyi et al. 2009			G1		**G5**	G7	**G10**				**G8**	
	Krieger et al. 2017										**tONa**		
	Nath & Schwartz 2017												**OFF-hOS**
	Jacoby et al. 2015		Suppr. by contrast										
	Tien et al. 2016		Suppr. by contrast										
	Jacoby et al. 2017					HD1, HD2							
Putative Function		Movement direction	Vertically oriented object	*Stable illuminaction*	Large moving objects	*Small, slow objects*	?	*Movement direction*	Expansion detector	Large moving objects	Small objects	Local motion	Horizontally oriented object

Supplemental Table 1: Putative retinal ganglion cell types and function. Extended version of Table 1 including also less likely candidates.